**Correspondence to:**

A. Roobaert,
alizee.roobaert@vliz.be

# Unraveling the Physical and Biological Controls of the Global Coastal CO2 Sink

Alizée Roobaert[1,2,3] , Laure Resplandy[2,4] , Goulven G. Laruelle[1] , Enhui Liao[2,5], and Pierre Regnier[1]

[1]Department of Geosciences, Environment & Society-BGEOSYS, Université Libre de Bruxelles, Brussels, Belgium, [2]Department of Geosciences, Princeton University, Princeton, NJ, USA, [3]Flanders Marine Institute (VLIZ), Ostend, Belgium, [4]High Meadows Environmental Institute, Princeton University, Princeton, NJ, USA, [5]School of Oceanography, Shanghai Jiao Tong University, Shanghai, China

**Abstract** The drivers governing the air-sea $CO_2$ exchange and its variability in the coastal ocean are poorly understood. Using a global ocean biogeochemical model, this study quantifies the influences of thermal changes, oceanic transport, freshwater fluxes, and biological activity on the spatial and seasonal variability of $CO_2$ sources/sinks in the global coastal ocean. We identify five typical coastal behaviors (dominated by biological drawdown, vertical transport, land imprint, intracoastal alongshore currents, and weak $CO_2$ sources and sinks coastal regions) and propose a new processed-based delineation of the coastal ocean based on the quantification of these controlling processes. We find that the spatiotemporal variability of $CO_2$ sources/sinks is dominated by strong exchanges with the open ocean and intracoastal processes, while continental influences are restricted to hotspot regions. In addition, where thermal changes appear to drive the seasonal $CO_2$ variability, it often results from compensating effects between individual non-thermal terms, especially biological drawdown and vertical transport.

**Plain Language Summary** Large progress has been made to further our understanding of the exchange of $CO_2$ between the atmosphere and the global coastal ocean. The complex interplay of physical and biogeochemical processes controlling these $CO_2$ fluxes as well as their variations in time and space are still, however, poorly quantified. This knowledge gap limits our understanding of how coastal regions respond to anthropogenic perturbations. This study aims at assessing the extent to which the spatial and seasonal variability of the $CO_2$ exchange between the global coastal ocean and the atmosphere is controlled by exchanges with the adjacent open ocean, the imprint of land inputs, or intracoastal processes. After a careful evaluation against an observation-based product of coastal air-sea $CO_2$ fluxes, the global biogeochemical model MOM6-COBALT is used to quantify the respective contributions of thermal changes, biological activity, freshwater influence as well as oceanic transport on the spatial and seasonal air-sea $CO_2$ dynamics for the coastal ocean worldwide. We identify five typical behaviors within coastal systems and delineate regions under the imprint of land, dominated by intracoastal alongshore currents, biological drawdown, vertical transport, and weak $CO_2$ sources/sinks coastal regions.

## 1. Introduction

Globally, the coastal ocean acts as a sink of carbon dioxide ($CO_2$) by taking up between 0.19 and 0.45 Petagrams of carbon from the atmosphere each year (Pg C yr$^{-1}$, Borges, 2005; Borges et al., 2005; Cai, 2011; C. T. A. Chen & Borges, 2009; C. T. A. Chen et al., 2013; Dai et al., 2013; Laruelle et al., 2010), with the latest estimates pointing toward the lower estimates (Dai et al., 2022; Regnier et al., 2022; Resplandy et al., 2024; Roobaert et al., 2019). This global uptake is the cumulated effect of strong coastal $CO_2$ sinks in temperate regions and at high latitudes, partially compensated by weak coastal $CO_2$ sources in sub-tropical and tropical regions (e.g., Borges et al., 2005; Cai, 2011; Cao et al., 2020; C. T. A. Chen et al., 2013; Dai et al., 2022; Laruelle et al., 2010, 2014; Resplandy et al., 2024; Roobaert et al., 2019). This large-scale latitudinal gradient suggests that sea surface temperature (SST) is a first order control on the sea surface partial pressure of $CO_2$ (called hereafter p$CO_2$) and hence on the coastal air-sea $CO_2$ flux (F$CO_2$) (e.g., Laruelle et al., 2014). However, strong variability at a smaller spatial scale, within a given latitudinal band, indicates that SST works in conjunction with other processes, such as the supply of dissolved inorganic carbon (DIC) by upwelling or the DIC consumption by biological activity, to control p$CO_2$ and F$CO_2$ (e.g., Laruelle et al., 2014).

While the spatial distribution of the coastal $FCO_2$ is now relatively well constrained thanks to the significant increase in field measurements (19 million of coastal $pCO_2$ data in the last release of the Surface Ocean $CO_2$ Atlas data product, SOCATv2022, Bakker et al., 2022) and the popularization of advanced interpolation techniques allowing the production of data driven spatially continuous monthly $pCO_2$ climatologies (Chau et al., 2022; Fay et al., 2021; Landschützer et al., 2020; Laruelle et al., 2017; Roobaert et al., 2024), on seasonal timescale its variability is less known at the global scale and only recently started to be investigated (e.g., Cao et al., 2020; Dai et al., 2022; Laruelle et al., 2014; Resplandy et al., 2024; Roobaert et al., 2019). At first order, $FCO_2$ seasonal amplitude is large at temperate and high latitudes and decreases equatorward. This seasonality in coastal $FCO_2$ is mainly governed by changes in $pCO_2$ although wind speed and sea-ice cover can also play an important role in some coastal regions, in particular at temperate and high latitudes (e.g., Arruda et al., 2015; Frankignoulle & Borges, 2001; Nakaoka et al., 2006; Roobaert et al., 2019; Shadwick et al., 2010, 2011; Turi et al., 2014; Yasunaka et al., 2016). In light of this emerging understanding, an important knowledge gap remains in the identification and quantification of the different processes and mechanisms responsible for these variations.

Quantification of the physical and biogeochemical processes that control the coastal $pCO_2$ and hence $CO_2$ sources/sinks and their seasonal variations has only been investigated regionally (e.g., Cao et al., 2020; Turi et al., 2014), and remains an open challenge at the scale of the global coastal ocean. The annual average and seasonal variations in $pCO_2$ have mostly been investigated through the decomposition into a thermal effect tied to SST changes and a non-thermal effect (combining the influences of changes in Alkalinity (ALK), sea surface salinity (SSS) and DIC), which is quantified as the residual between the thermal effect and the net change in $pCO_2$ (see Takahashi et al., 1993). Using this method, studies relying on observational time-series from 10 buoys located along the U.S coasts (S. Chen & Hu, 2019), from global but discrete $pCO_2$ data from the SOCAT database (Cao et al., 2020) or from a global continuous monthly resolved $pCO_2$ climatology derived from in situ sea surface $CO_2$ observations (Laruelle et al., 2017), have suggested that the coastal $pCO_2$ seasonality broadly follows that of the neighboring open ocean. These analyses suggested that non-thermal effects control $pCO_2$ seasonality at temperate and high latitudes, whereas the thermal effect is the main controlling factor at low latitudes (tropical and subtropical regions), except in coral reef ecosystems and river and upwelling dominated shelves where non-thermal processes are the main control (e.g., Cao et al., 2020; S. Chen & Hu, 2019; Laruelle et al., 2017).

To investigate non-thermal effects further, Cao et al. (2020) and Dai et al. (2022) established a simple mass balance equation allowing to distinguish two distinct regimes in the $CO_2$ flux dynamics: the river-dominated ocean margins ("RiOMar"), where the carbon fluxes are primarily controlled by terrestrial loads and thermo-dynamics effects associated with change in SSS (see e.g., Abril et al., 2021), and ocean-dominated margin ("OceMar") where the carbon fluxes are primarily controlled by exchanges with the surrounding open ocean. In RiOMar systems (McKee et al., 2004; Rabouille et al., 2001), the $CO_2$ flux dynamics results from the ratio between terrestrial nutrient loads (which promote biological photosynthetic activity) relative to terrestrial dissolved organic matter loads (which promotes biological remineralization). In OceMar (Dai et al., 2013), the $CO_2$ flux dynamics result from open ocean nutrient and DIC inputs via horizontal circulation and vertical exchanges (mixing and upwellings). This method has successfully been applied to three coastal regions in Cao et al. (2020) and to seven coastal regions in Dai et al. (2022) and provides a semi-quantitative view of the underlying processes driving the $CO_2$ dynamics but groups the ocean-dominated shelves into a single category although distinct behaviors have been documented (e.g., Fennel & Wilkin, 2009; Frischknecht et al., 2018; Laruelle et al., 2015). The $CO_2$ flux dynamics in the coastal ocean was also investigated by Cai et al. (2006) and Cai (2011) using a conceptualization of the coastal ocean into three types of coastal systems (Western and Eastern boundary currents and polar coastal region) and seven provinces (Antarctic, Arctic, eutrophic, mesotrophic, low-latitude Western boundary current, low and mid-latitude Eastern boundary current). These provinces were defined using both physical and biological properties (e.g., difference in ocean circulation, latitude, morphology, primary productivity) which potentially influence DIC dynamics as suggested in prior work (e.g., Ducklow & McCallister, 2004; Walsh, 1988; Wollast, 1998). With this approach, Cai et al. (2006) and Cai (2011) aimed to provide a reliable estimation of global coastal $FCO_2$ through the collection and synthesis of available data-driven local $FCO_2$ estimates in each type of system and their extrapolation over the surface areas of each province.

K. Liu et al. (2010) proposed a finer classification accounting for climatic conditions and boundary currents, dividing the coastal ocean into polar, subpolar, and tropical shelves, Eastern boundary currents, Western boundary currents, monsoon dominated shelves and marginal coastal seas. However, the geographical limits of each class were not clearly defined, and the segmentation mostly relied on physical criteria. This classification

was subsequently used as a basis of the MARCATS segmentation (for MARgins and CATchments Segmentation, Laruelle et al., 2013), which divides the global coastal ocean into 45 units based on hydrological, climatic, and geomorphological properties. The MARCATS segmentation has been used since then to investigate for example, the residence time of coastal waters (e.g., X. Liu et al., 2019) and to investigate the carbon dynamics of the coastal ocean (e.g., Bourgeois et al., 2016; C. T. A. Chen et al., 2013; Dai et al., 2022; Lacroix et al., 2020; Laruelle et al., 2014; Roobaert et al., 2019) despite still not being constrained by the spatiotemporal distribution of the physical and biogeochemical processes controlling the carbon and $CO_2$ dynamics in the global coastal ocean. For instance, Roobaert et al. (2022) identified a significant biogeochemical heterogeneity within individual MARCATS and the broad shelf classes by K. Liu et al. (2010).

In parallel to these efforts to construct global conceptual coastal typologies capturing the different $CO_2$ dynamics, process-based models of the global coastal ocean carbon cycle have been developed over the last two decades. Conceptual box models were first developed (e.g., Mackenzie et al., 2002, 2012; Rabouille et al., 2001; Ver et al., 1999) to investigate the long-term evolution of the global coastal $FCO_2$, suggesting a shift from a net $CO_2$ source under pre-industrial conditions to a present-day net $CO_2$ sink induced by atmospheric $CO_2$ increase and the impact of enhanced nutrient inputs from the land on the coastal biological carbon pump (e.g., Mackenzie et al., 2002). However, the response of the biological carbon pump was highly uncertain in these highly idealized simulations (Regnier et al., 2013), ignoring the highly heterogeneous character of the global coastal ocean. In recent years, global ocean biochemical models have increasingly been applied to resolve the global coastal ocean carbon cycle (Bourgeois et al., 2016; Lacroix et al., 2020, 2021a, 2021b; Mathis et al., 2022; Roobaert et al., 2022). These models overall revealed much stronger exchanges with the open ocean, leading to significantly shorter water residence times on the shelves (Lacroix, Ilyina, Laruelle, & Regnier, 2021; X. Liu et al., 2019) than previously found with box-models, and a weaker imprint of the land on the coastal carbon dynamics. In addition, long-term simulations hint at a weaker anthropogenic perturbation, suggesting that the global coastal ocean may already have been a $CO_2$ sink during pre-industrial times (Lacroix, Ilyina, Laruelle, & Regnier, 2021; Regnier et al., 2022).

These global ocean biogeochemical model simulations provided useful insights into the underlying physical and biogeochemical processes responsible for the century-scale evolution of the air-sea $CO_2$ exchange. However, they did not address the extent to which the same processes control the spatial and seasonal variability in the global coastal $CO_2$ fluxes. Only regional scale model applications (e.g., Arruda et al., 2015; Turi et al., 2014; Yasunaka et al., 2016) have decomposed the $pCO_2$ seasonality into changes induced by thermal effects, biological activity, oceanic circulation, and the air-sea $CO_2$ exchange itself. For instance, Turi et al. (2014) found that coastal $pCO_2$ seasonality in the California Current was dominated by the oceanic circulation while Arruda et al. (2015) found that the thermal effect and biological activity dominate the seasonal signal in the Patagonian shelf.

This study aims to fill the gaps in our understanding of the different drivers that govern the $CO_2$ spatial and seasonal variability for the coastal regions worldwide. More specifically, our objectives are three-fold:

- Quantify the respective contributions of freshwater inputs, ocean circulation and biological activity by determining the spatial variability in global coastal $CO_2$ sources/sinks
- Quantify the respective contributions of thermal effects, freshwater inputs, ocean circulation and biological activity on the seasonal variability of the global coastal $CO_2$ exchange
- Propose a new delineation of the global coastal ocean based on the quantification of the internal control mechanisms of the coastal $CO_2$ dynamics.

To do so, we leverage the method described in Roobaert et al. (2022), which refines the traditional Takahashi et al. (1993) decomposition to more robustly capture the highly variable $CO_2$ dynamics encountered in coastal waters. We evaluate the global ocean biogeochemical model MOM6-COBALT against the observational $pCO_2$-based product of Laruelle et al. (2017). We then use it to simulate the spatiotemporal $FCO_2$ coastal dynamics and its decomposition into the underlying physical and biogeochemical processes driving the exchange, as illustrated by Roobaert et al. (2022) for three well studied coastal regions. This study provides a spatiotemporally explicit global application of this approach, allowing for the quantification of the different processes and mechanisms responsible for the $FCO_2$ variability in the global coastal ocean.

## 2. Methods

### 2.1. Coastal Air-Sea $CO_2$ Exchange

We use simulations obtained from the Geophysical Fluid Dynamics Laboratory global ocean/sea-ice Modular Ocean Model version 6 (MOM6, Adcroft et al., 2019) coupled to the biogeochemical module Carbon Ocean Biogeochemistry And Lower Trophics version 2 (COBALTv2, Stock et al., 2014, 2020) to simulate the coastal ocean $FCO_2$ at a nominal horizontal resolution of 0.5° globally (0.5° for longitude, 0.25°–0.5° for latitude). The ocean carbonate chemistry in COBALTv2 uses the Model the Ocean Carbonate System (Mocsy 2.0, Orr & Epitalon, 2015). A detailed description of the model can be found in Text S1 of Supporting Information S1 as well as in Liao et al. (2020) and Roobaert et al. (2022). Our model results are evaluated against a coastal $FCO_2$ product derived from the monthly 0.25° continuous $pCO_2$ coastal product of Laruelle et al. (2017). This observation-based climatology was generated by a two-step artificial neural network interpolation technique relying on 13.6 million measurements extracted from the SOCATv4 database (Bakker et al., 2016) for the 1998–2015 period. For both products, $FCO_2$ (mol C m$^{-2}$ yr$^{-1}$) is calculated using the following formulation:

$$FCO_2 = k \, K_0 \left(1 - f_{ice}\right) \Delta pCO_2 \tag{1}$$

where $\Delta pCO_2$ is the air-sea $pCO_2$ difference (atm), $K_0$ is the SST- and SSS-dependent $CO_2$ solubility constant (mol C m$^{-3}$ atm$^{-1}$), $f_{ice}$ is the sea-ice fraction coverage (no unit) and $k$ is the wind speed dependent gas exchange transfer velocity (m yr$^{-1}$, see Text S2 in Supporting Information S1 for a detailed description). Positive $FCO_2$ values are a $CO_2$ source to the atmosphere. The modeled $FCO_2$ uses $\Delta pCO_2$ computed by MOM6-COBALT (regridded to the 0.25° observation-based $FCO_2$ grid) and is calculated online, that is, $\Delta pCO_2$ and the wind speed dependent gas exchange transfer velocity term are updated at each time step of the model and thus coupled to one another. A larger value of $k$ reduces the $pCO_2$ gradient at the air-water interface and thus the $CO_2$ flux. The observation-based $FCO_2$ is however calculated offline and there cannot be any compensatory effects between the different terms in Equation 1. The monthly $FCO_2$ maps calculated online using MOM6-COBALT are the integration of shorter time scale calculations by the model, while the calculations performed using the observation-based product rely on monthly mean values. However, to minimize the bias possibly associated with this difference, both observation-based and modeled $FCO_2$ are calculated using the same k-relationship versus wind speed that is, the one from the model which is based on the parameterization of Wanninkhof (1992) and the wind speed from JRA55-do v1.3 (Tsujino et al., 2018). $K_0$ is computed using observed SST and SSS in the observation-based $FCO_2$, while it is computed using simulated SST and SSS in the model (see Text S2 in Supporting Information S1). The sea-ice cover is from observed sea-ice (Cavalieri et al., 1996) for the observation-based $FCO_2$, while it is modeled by the sea-ice model SIS2 in MOM6-COBALT (Adcroft et al., 2019). For the modeled $FCO_2$, the atmospheric $pCO_2$ is derived from the latitudinally and -temporally varying atmospheric $pCO_2$ dataset from the Earth System Research Laboratory (ESRL, Joos & Spahni, 2008). For the observation-based $FCO_2$ product, the atmospheric $pCO_2$ is derived from the SeaFlux product (Fay et al., 2021). The difference in atmospheric $pCO_2$ between the product used for the model calculation (ESRL) and the observation-based calculation (SeaFlux) is however very small and significantly smaller than the magnitude of the $pCO_2$ gradient used to calculate $FCO_2$.

The coastal domain is defined here following Laruelle et al. (2017) using a global mask that excludes estuaries and inland water bodies and covers a total surface area of 77 million km$^2$. The outer limit of the coastal domain is set by whichever point is the furthest from the shoreline between the 1,000 m isobath and a fixed 300 km distance (roughly the outer edge of territorial waters). The spatiotemporal differences observed between the model and the observation-based $FCO_2$ product (see Sections 3.1 and Figure S2 in Supporting Information S1) can be largely attributed to differences in ocean $pCO_2$ since we use the same k-parameterization and wind product (see Text S2 in Supporting Information S1). In contrast, the influence of other parameters (e.g., the sea-ice coverage, $K_0$, see Equation 1) is small compared to the one associated with $pCO_2$ (see Text S2 and Figure S3 in Supporting Information S1; e.g., Roobaert et al., 2018, 2024; Wanninkhof, 2014).

The model performance and its ability to simulate the spatiotemporal $pCO_2$ dynamics is extensively discussed in Roobaert et al. (2022) in which a detailed model-data comparison at global scale and for each of the 45 units of the MARCATS segmentation of Laruelle et al. (2013) is presented. This comparison was performed against raw $pCO_2$ data from the SOCAT database as well as the observation-based $pCO_2$ of Laruelle et al. (2017). The model performance was also evaluated against in situ observations for several environmental parameters that are known

to control pCO$_2$ and thus the CO$_2$ flux such as SST, SSS and sea surface nutrients (i.e., silicates, phosphate, and nitrate). Results from Roobaert et al. (2022) showed that for most coastal regions, the model reproduces the spatial and temporal variability of pCO$_2$ and environmental variables. In this manuscript, the model was further evaluated against DIC and ALK data (see Text S3 and Figures S4–S6 in Supporting Information S1).

Based on several evaluation criteria (i.e., annual average pCO$_2$ mismatch <20 µatm, Pearson correlation coefficient >0.5 on their pCO$_2$ seasonal cycles, and seasonal pCO$_2$ amplitude mismatch <20 µatm), Roobaert et al. (2022) identified regions of agreement and strong mismatch between MOM6-COBALT and the observation-based annual mean pCO$_2$ and seasonal cycles using the MARCATS segmentation (dotted regions in Figure S7 of Supporting Information S1 correspond to strong mismatch, see Roobaert et al. (2022) for details). Regions of strong mismatch mainly correspond to semi-enclosed seas, also defined as marginal seas in the classification of K. Liu et al. (2010), for example, the Baltic Sea, the Mediterranean Sea, or the Sea of Japan, for which a strong mismatch was also observed between the model output and some other environmental variables (i.e., SSS, SST, sea surface nutrients; see Roobaert et al., 2022). Due to these strong model-data disagreement and the complex nature of these semi-enclosed seas which are particularly difficult to simulate for a global oceanic model such as MOM6, we decided to not discussed these regions when investigating the respective contributions of the different processes determining the annual mean and seasonal FCO$_2$ variability (i.e., the Hudson Bay, the Baltic, the Mediterranean, the Black, and the Red seas, the Persian Gulf, the Sea of Japan, and the Sea of Okhotsk). 6 other MARCATS regions were characterized by Roobaert et al. (2022) as regions of strong model-data pCO$_2$ mismatch: the Peruvian upwelling current, the West Arabian Sea, the Bay of Bengal, the Sea of Labrador, the New Zealand, in the Tropical East Pacific and SE of Asia. These regions should be considered with caution, but we decided to include them in the process of decomposition analysis since it is difficult to assess if the mismatch between the model and the observation-based product really corresponds to poor performance of the model itself or weakness of the data product in data-poor areas (Roobaert et al., 2022). Indeed, most of these regions are scarcely sampled in the SOCAT database (see Figure S7 in Supporting Information S1) and/or represent regions of complex dynamics of biogeochemical settings (e.g., upwelling, sea-ice coverage, …) for which the observation-based pCO$_2$ suffers from poor performance (Laruelle et al., 2017; Roobaert et al., 2022).

### 2.2. Contribution of Ocean Processes to the Coastal CO$_2$ Response

Surface ocean pCO$_2$ responds to changes in DIC, ALK, SST, and SSS associated with physical and biological processes (Sarmiento & Gruber, 2006; Wolf-Gladrow et al., 2007). We use the decomposition method developed by Liao et al. (2020) and adapted for coastal regions in Roobaert et al. (2022) to quantify how ocean processes influence the oceanic CO$_2$ response (noted "CResponse"):

$$
\underbrace{\partial_t pCO_2 - \left(\frac{\partial pCO_2}{\partial DIC}\partial_t DIC_{CO_2\ flux}\right)}_{CResponse} \approx \underbrace{\frac{\partial pCO_2}{\partial SST}(\partial_t SST_h + \partial_t SST_v + \partial_t SST_q)}_{thermal}
$$

$$
+ \underbrace{\underbrace{\left(\frac{\partial pCO_2}{\partial DIC}\partial_t DIC_{bio} + \frac{\partial pCO_2}{\partial ALK}\partial_t ALK_{bio}\right)}_{bio} + \underbrace{\left(\frac{\partial pCO_2}{\partial DIC}\partial_t DIC_v + \frac{\partial pCO_2}{\partial ALK}\partial_t ALK_v + \frac{\partial pCO_2}{\partial SSS}\partial_t SSS_v\right)}_{Vcirc}}_{vert.\ biophysical\ dyn.}
$$

$$
+ \underbrace{\underbrace{\left(\frac{\partial pCO_2}{\partial DIC}\partial_t DIC_{fw} + \frac{\partial pCO_2}{\partial ALK}\partial_t ALK_{fw} + \frac{\partial pCO_2}{\partial SSS}\partial_t SSS_{fw}\right)}_{FW} + \underbrace{\left(\frac{\partial pCO_2}{\partial DIC}\partial_t DIC_h + \frac{\partial pCO_2}{\partial ALK}\partial_t ALK_h + \frac{\partial pCO_2}{\partial SSS}\partial_t SSS_h\right)}_{Hcirc}}_{FW\ and\ lateral\ trans.}
$$

$$(2)$$

The Left-Hand Side (LHS) of Equation 2 represents the oceanic $CO_2$ response ("*CResponse*," see Table S1 in Supporting Information S1) which includes two contributions: (a) the air-sea $CO_2$ flux ($\frac{\partial pCO_2}{\partial DIC}\partial_t DIC_{CO_2 \text{ flux}}$) which acts to compensate for changes in DIC by exchanging with the atmosphere, and (b) the residual $pCO_2$ change over the period considered ($\partial_t pCO_2$) which arises from the fact that the ocean and the atmosphere are not equilibrated on seasonal timescales ($CO_2$ equilibration timescale of ∼10 months for a Mixed Layer Depth (MLD) of 50 m, see Sarmiento & Gruber, 2006). On average between 1998 and 2015, the air-sea flux almost equilibrates the changes in $pCO_2$ tied to the Right-Hand Side (RHS) (i.e., $\partial_t pCO_2 \cong 0$) and the $CO_2$ response therefore nearly equates the air-sea $CO_2$ flux (CResponse $\cong \frac{\partial pCO_2}{\partial DIC}\partial_t DIC_{CO_2 \text{ flux}}$), the small difference between the two being explained by inter-annual variability. On seasonal timescales, however, both the air-sea $CO_2$ flux and $\partial_t pCO_2$ contribute to the $CO_2$ response.

The RHS of Equation 2 represents the ocean processes that affect $pCO_2$ through changes in ALK, DIC, SSS, and SST. The thermal effect (noted "*thermal*") includes changes in SST associated with horizontal oceanic transport (advection, and diffusivity in the meridional and zonal directions, noted $\partial_t SST_h$), vertical oceanic transport (vertical advection and diffusivity, $\partial_t SST_v$) and the effect of the surface heat flux ($\partial_t SST_q$). The thermal effect here includes all processes influencing temperature in the ocean. This contrasts with other decomposition methods (e.g., Lauderdale et al., 2016) in which the thermal effect is defined as the influence of air-sea heat flux alone, while thermal changes due to ocean circulation are combined into a residual with other terms. Separating air-sea heat fluxes from ocean heat transport in their effect on DIC overestimates the impact of thermal changes as the two processes largely compensate each other (for instance, mixed-layer warming due to advection/mixing is rapidly compensated by air-sea heat loss to the atmosphere e.g., Liao et al., 2020).

The term noted "*bio*" denotes the DIC and ALK changes induced by biological processes (photosynthesis/respiration, calcium carbonate dissolution/precipitation and denitrification/nitrification). Changes in chemical species (DIC, ALK, and SSS) associated with the vertical oceanic transport (advection and mixing) are represented by the term noted "*Vcirc*." Grouped together, the sum of *bio* and *Vcirc* represents the net changes in chemical species by vertical biophysical dynamics (noted "*vert. biophysical dyn.*") and provides insight on whether the biological drawdown or the vertical supply control this local balance. Changes in DIC, ALK, and SSS associated with lateral transport and dilution/concentration effects by freshwater (i.e., precipitation/evaporation, river runoff and sea-ice formation/melting) are represented by the "*Hcirc*" and the "*FW*" terms, respectively. We grouped together these two terms (noted "*FW and lateral trans.*") to isolate the influence of the *thermal* effect and the *vertical biophysical dynamics* from the other processes. Further details about the method including the coefficients used for the $pCO_2$ dependency on DIC, ALK, SST, and SSS ($\frac{\partial pCO_2}{\partial DIC}$, $\frac{\partial pCO_2}{\partial ALK}$, $\frac{\partial pCO_2}{\partial SST}$, and $\frac{\partial pCO_2}{\partial SSS}$), the model configuration, spin-up, simulation protocol and decomposition method can be found in Text S1 of Supporting Information S1 as well as in Liao et al. (2020) and in Roobaert et al. (2022).

The contribution of the different mechanisms on the RHS of Equation 2 to the oceanic $CO_2$ response was quantified on the 0.25° grid. All variables were averaged between the sea surface and the MLD, defined here as the depth where the water density is 0.01 kg m$^{-3}$ denser than the water at the surface (minimum MLD of 5 m). On annual timescales, the relative contribution between the *thermal effect*, the *vertical biophysical dynamics* and the *freshwater and lateral transport* is calculated as the fraction of the $CO_2$ response associated with each process. On seasonal timescales, we first perform linear regressions of the monthly seasonal anomaly of process $x$ onto the monthly seasonal anomaly of the $CO_2$ response and evaluate the slopes $\beta$ for each process (e.g., $\beta_{\text{thermal}}$ for the *thermal* contribution). Our simple linear regression method shows that over 83% of the coastal grid cells, the $r^2$ of the dominant process is >0.5 (see Figure S8 in Supporting Information S1). Due to the nonlinear dependence of the different terms used in Equation 2, however, the sum of the three $\beta$s is not perfectly equal to 1. We thus quantify the relative contribution of each process by normalizing the sum of the three absolute values of $\beta$ to 1 and recalculate the relative contribution of each of the three processes (see Figure S9 in Supporting Information S1). Next, we associate the dominance of one process or the co-dominance of two or the three processes based on a color ternary diagram with a threshold of 30%. Based on this reconstructed ternary plot, each pixel is associated with its corresponding color.
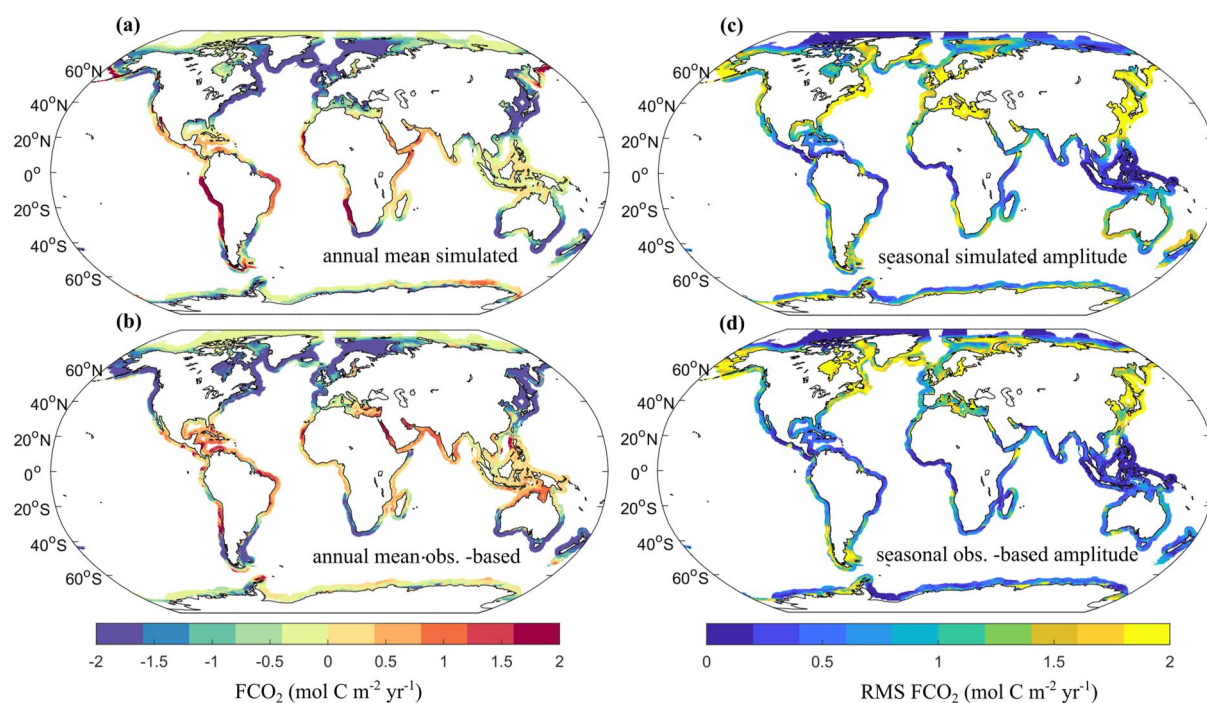
**Figure 1.** Annual average air-sea $CO_2$ flux ($FCO_2$, mol C m$^{-2}$ yr$^{-1}$) (a) simulated by the MOM6-COBALT model and (b) based on observations. Seasonal $FCO_2$ amplitude (root mean square, RMS, of their monthly anomalies, mol C m$^{-2}$ yr$^{-1}$) in the (c) model and the (d) observation-based product. Further information on their comparison can be found in Figure S2 of Supporting Information S1 and in Section 3.1.

## 3. Results

### 3.1. Coastal Air-Sea $CO_2$ Exchange Spatial and Seasonal Variability in Model and Product

The MOM6-COBALT model reproduces the spatial distribution of the annual average air-sea $CO_2$ flux ($FCO_2$) obtained from the observation-based $pCO_2$ product coastal SOM-FFN (Figures 1a and 1b). In both the MOM6-COBALT model and the observation-based product, the global coastal $CO_2$ flux amounts to −0.6 Pg C yr$^{-1}$ (negative flux into the ocean) over the 1998–2015 period and an extended coastal area of $77 \times 10^6$ km$^2$. Note that the observations-based $FCO_2$ value of −0.6 Pg C yr$^{-1}$ is larger than the one calculated by Roobaert et al. (2019, value of −0.2 Pg C yr$^{-1}$) because of the larger coastal area ($77 \times 10^6$ km$^2$ here vs. $28 \times 10^6$ km$^2$ in Roobaert et al., 2019) and the different wind speed and gas exchange coefficient parameterization used here (see Text S2 and Figure S1 in Supporting Information S1 for further details). Coastal $CO_2$ sources are largely located in the tropics and subtropics (40°S–40°N), while $CO_2$ sinks are found at temperate (between 40° and 60° of latitude) and high (poleward of 60°) latitudes in both hemispheres (Figures 1a and 1b), in agreement with prior studies (e.g., Borges et al., 2005; Cai, 2011; C. T. A. Chen et al., 2013; Dai et al., 2022; Laruelle et al., 2010, 2014; Resplandy et al., 2024; Roobaert et al., 2019). The strongest $CO_2$ sources ($FCO_2$ values > 0.5 mol C m$^{-2}$ yr$^{-1}$) are mainly encountered along upwelling currents, while the strongest sinks ($FCO_2$ values <−0.5 mol C m$^{-2}$ yr$^{-1}$) mainly occur in temperate and high latitudes of the Northern Hemisphere, along river plumes (e.g., the Amazon River) as well as along intracoastal alongshore currents (e.g., the Gulf stream). The weak sources/sinks (absolute $FCO_2$ values <0.5 mol C m$^{-2}$ yr$^{-1}$) are mainly found along the tropical band and at high latitudes of both hemispheres. In most of the coastal domain (72% of the coastal surface area), the absolute difference between the model and the observation-based air-sea $CO_2$ flux density is smaller than 1 mol C m$^{-2}$ yr$^{-1}$ and large differences (>2 mol C m$^{-2}$ yr$^{-1}$) occur in poorly monitored regions such as the Peruvian upwelling Current, the Sea of Okhotsk, or in the Hudson Bay (Figures S2a–S2c in Supporting Information S1).

The model also captures seasonal variations in $FCO_2$ (estimated by the root mean square (RMS) of monthly values) similar in magnitude to the coastal observation-based $pCO_2$ product (absolute model-product RMS mismatch <0.5 mol C m$^{-2}$ yr$^{-1}$ over 62% of the coastal area, Figures 1c and 1d; Figures S2d–S2f in Supporting Information S1). In particular, the model reproduces the general pattern of large amplitudes in temperate and high

latitude regions (seasonal RMS >0.8 mol C m$^{-2}$ yr$^{-1}$) compared to low latitudes (<0.8 mol C m$^{-2}$ yr$^{-1}$), also in line with prior work that highlighted this latitudinal contrast in coastal seasonality (e.g., Roobaert et al., 2019). Large seasonal amplitudes are also simulated by the model along upwelling currents and at the mouth of several rivers such as the Amazon plume. The model also generally captures the observed seasonal timing of FCO$_2$ in 71% of coastal grid cells (Pearson correlation coefficients >0.5 between modeled and observation-based seasonal cycles), with some notable exceptions such as in Southeast Asia and along sections of the eastern boundary upwelling systems in the South Pacific and South Atlantic Ocean (Figure S2g in Supporting Information S1). These regions of phase mismatch, however, generally have very small seasonal amplitudes (e.g., RMS <0.1 mol C m$^{-2}$ yr$^{-1}$ in Southeast Asia, Figures S2d and S2e in Supporting Information S1) and/or poor observational coverage in the SOCAT database (lower than 30%, Figure S7 in Supporting Information S1), suggesting that these apparent model-product differences either have a small influence on the coastal carbon dynamics or are poorly constrained by available observations. Nevertheless, the potential limitations of both the model and the pCO$_2$ product in eastern boundary upwelling systems should be kept in mind. Although the spatial resolution of our model (0.25°–0.5°) cannot explicitly resolve small-scale circulation processes, the relatively good match between the model and the data product found on annual average and on seasonal timescales lends confidence in its ability to capture the processes controlling the coastal CO$_2$ dynamics worldwide.

### 3.2. Coastal Systems Classification Based on the Internal Control of the CO$_2$ Dynamics

We examine the processes that control the spatial and seasonal patterns of the coastal ocean CO$_2$ response (referred as the *CResponse*), which includes all pCO$_2$ changes, those equilibrated by the air-sea CO$_2$ flux and those remaining as residual pCO$_2$ changes (see Equation 2). We quantify the influence of *vertical biophysical dynamics* (vert. biophysical dyn.), *freshwater and lateral transport* (FW and lateral trans.) and *thermal changes* (see Equation 2) on annual and seasonal timescales (Figures 2 and 3).

The *vertical biophysical dynamics* term groups together changes in coastal pCO$_2$ resulting from biological activity (*bio*) and vertical transport (*Vcirc*) of chemical species (DIC, ALK and SSS), which are intimately linked and largely offset each other (annual average in Figure 2c and seasonality in Figure 3c, see Texts S4 and S5 in Supporting Information S1). Indeed, on an annual average, biological activity reduces the CO$_2$ response everywhere by consuming DIC (global median coastal value of *bio* = −292 µatm yr$^{-1}$, Figure 2e), while the vertical transport of chemical species increases the CO$_2$ response globally due to the supply of DIC to the mixed layer (global coastal median value of *Vcirc* = +225 µatm yr$^{-1}$, Figure 2g). Vertical transport also supplies nutrients that sustain biological activity, further reinforcing the link between these two terms (see Text S4 in Supporting Information S1 for further details). Similarly, on seasonal timescales, the variability associated with the transport of chemical species by vertical circulation is intimately linked with biological activity (contrast Figures 3e and 3g). We also consider the combined contributions of *freshwater and lateral transport* (FW and lateral trans., Figures 2d and 3d), which include dilution/concentration effects (e.g., evaporation, precipitation, runoff, fresh water (*FW*) term) and horizontal transport of chemical species (*Hcirc*). It should be noted that lateral transport can propagate local anomalies tied to other processes (e.g., *bio*, *Vcirc*, …) to surrounding areas through horizontal circulation. For instance, freshwater fluxes and lateral transport are intimately linked to one another in regions where low pCO$_2$ values tied to runoff discharge and dilution are transported to the surrounding regions by horizontal circulation (see Figures 2f, 2h, 3f, and 3h). Finally, we consider thermal changes (*thermal*), which only have a marginal impact on the oceanic CO$_2$ response on annual timescales (median thermal effect of −0.2 µatm yr$^{-1}$ on global coastal annual CO$_2$ response, Figure 2b) but influence the seasonality via spring/summer warming and fall/winter cooling (Figure 3b and Text S5 in Supporting Information S1). Note that the CO$_2$ response shown in Figure 2a equates the mean air-sea CO$_2$ flux (FCO$_2$) when averaged on annual timescales (pCO$_2$ changes are equilibrated on annual timescales, see method Section 2.2). From this process-based analysis, we identify five coastal systems, namely (a) coastal regions under the imprint of land, (b) intense coastal sources dominated by *vertical biophysical dynamics* (upwelling systems), (c) intense coastal sinks dominated by *vertical biophysical dynamics* (subpolar and polar systems), (d) intense coastal sinks dominated by lateral transport (intracoastal currents) and (e) weak coastal CO$_2$ sources and sinks, that we describe in Sections 3.2.1–3.2.5.

### 3.2.1. Coastal Regions Under the Imprint of Land

From our annual average process-based analysis (Figure 4a), we first isolate coastal regions that are under the influence of land-derived inputs using the annual maximum extension of low salinity river plumes (i.e., cells with
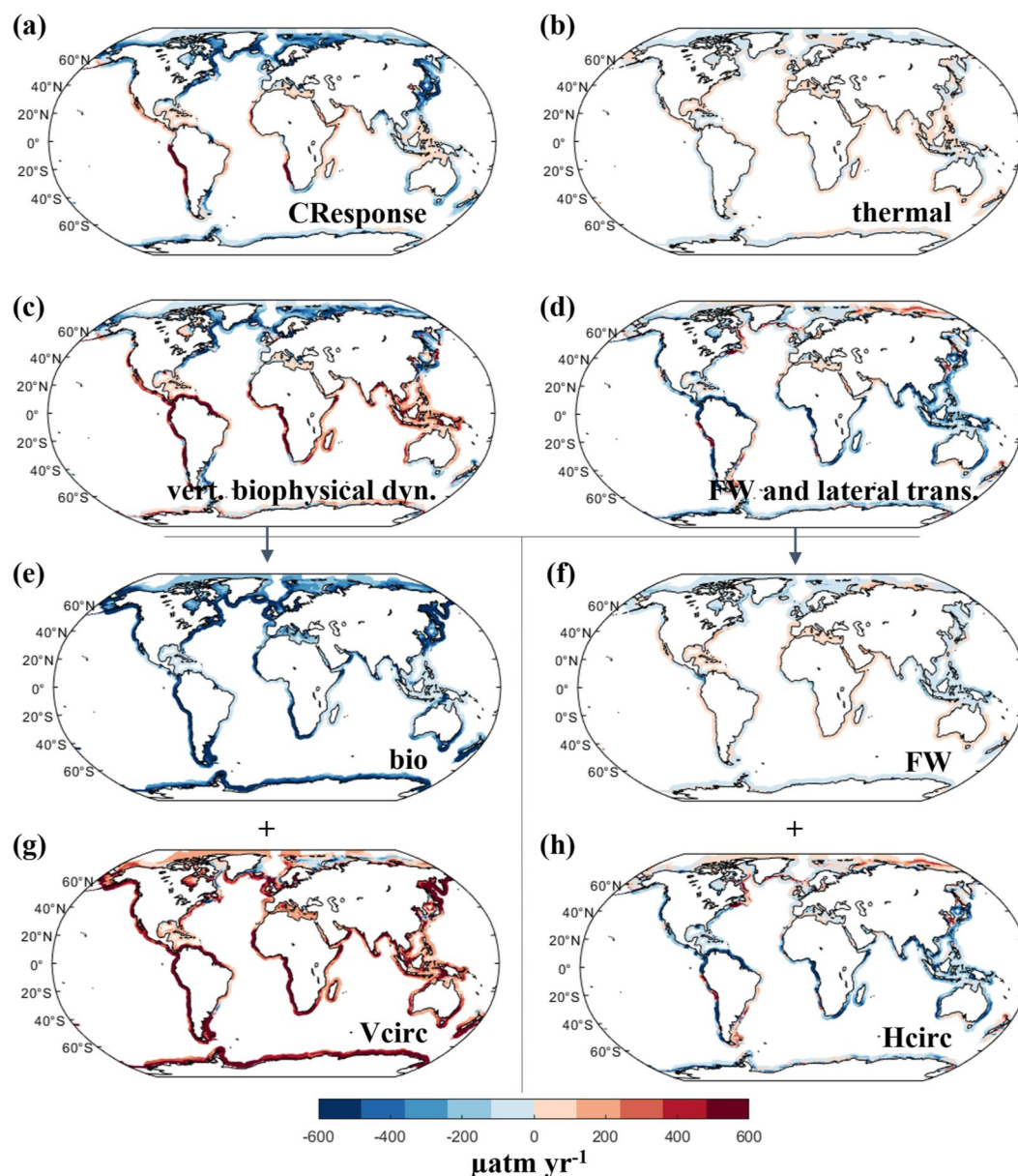
**Figure 2.** Annual average (a) oceanic $CO_2$ response (*CResponse*, includes changes in surface ocean $pCO_2$ and the associated air-sea $CO_2$ flux), contributions to this $CO_2$ response from the thermal change (*thermal*, b), the *vertical biophysical dynamics* (*vert. biophysical dyn.*, c), which represent the sum of biological activity (*bio*, e) and the vertical transport of chemical species by oceanic circulation (*Vcirc*, g). The contribution of *freshwater and lateral transport* (*FW and lateral trans.*, d) represents the sum of the dilution/concentration from freshwater fluxes (*FW*, f) and the transport of chemical species by horizontal circulation (*Hcirc*, h). The residual between *CResponse* and the sum of processes (b, e–h) can be found in Figure S10 of Supporting Information S1. Positive values (red colors) indicate an increase in $CO_2$ response and an outgassing to the atmosphere. All Panels are expressed in $\mu$atm yr$^{-1}$. See Text S4 in Supporting Information S1 for a description of the figure.

SSS anomalies 95% below the values of adjacent cells using a moving mean SSS calculated on a 20° longitude by 20° latitude window). These regions under strong land influence represent less than 10% of the global coastal surface area (6 million km$^2$, Figure 4b), a surface area slightly larger (some SSS anomalies may be a consequence of seasonal sea-ice melt) than the one calculated by Kang et al. (2013) using a similar approach to evaluate the global cumulated surface area of river plumes (between 3 and 5 million km$^2$ depending on the season). Examples of river plume regions include the northern Bay of Bengal, the mouth of the Amazon River, the mouth of the McKenzie River as well as the high latitude coastal regions located along the largest Eurasian rivers. These regions are generally intense $CO_2$ sinks (FCO$_2$ < −0.5 mol C m$^{-2}$ yr$^{-1}$ in Figure 1a) in which the contributions of
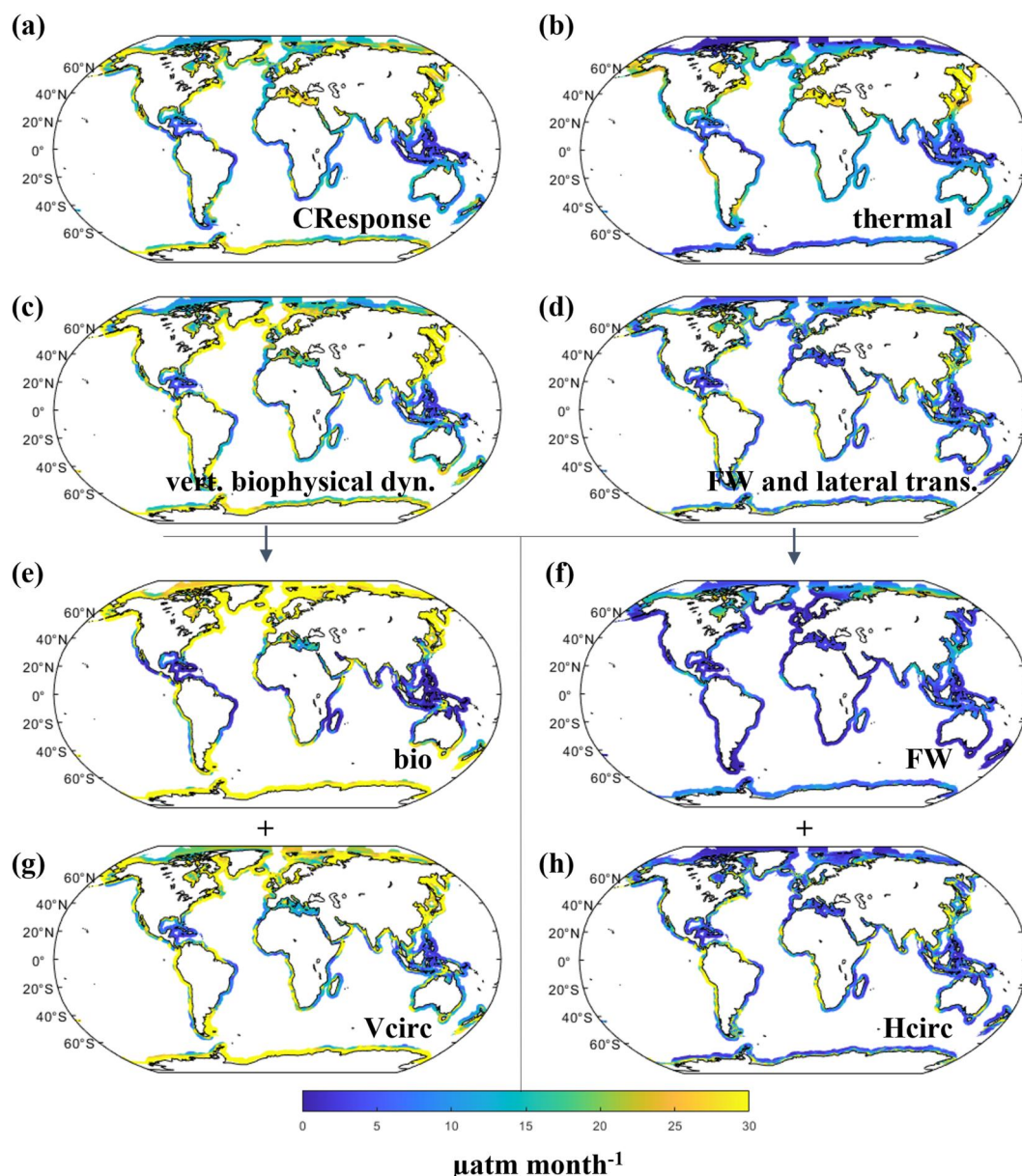
**Figure 3.** Amplitude of the variability on seasonal timescale (root-mean-square (RMS) of the monthly anomalies, in µatm month$^{-1}$) for (a) the $CO_2$ response (*CResponse*), (b) *thermal* change, (c) the *vertical biophysical dynamics* (vert. biophysical dyn., sum of *bio* (e) and *Vcirc* (g)) and (d) *freshwater and lateral transport* (FW and lateral trans., sum of *FW* (f) and *Hcirc* (h)). See Text S5 in Supporting Information S1 for a description of the figure.

both *freshwater and lateral transport* and *vertical biophysical dynamics* are important (gray colors when both contributions are of similar magnitude, Figure 4b). In these systems, the freshwater discharge (Figure S11b in Supporting Information S1) dilutes seawater and hence increases the $CO_2$ uptake (e.g., typical *FW* values around −200 µatm yr$^{-1}$ but that can reach −3,028 µatm yr$^{-1}$ very near river mouths such as in the Amazon plume, Figure 2f and Figure S12 in Supporting Information S1). Rivers also supply nutrients enhancing primary productivity as well as $CO_2$ uptake (e.g., *bio* value < −500 µatm yr$^{-1}$ in Amazon River plume, Figure 2e), a result consistent with previous studies (e.g., Araujo et al., 2017; Lefèvre et al., 2010; Louchard et al., 2021; Valerio et al., 2021).

On a seasonal timescale, the variability of coastal regions under the influence of large riverine plumes is also generally dominated by seasonal changes in the *freshwater and lateral transport* and the *vertical biophysical*
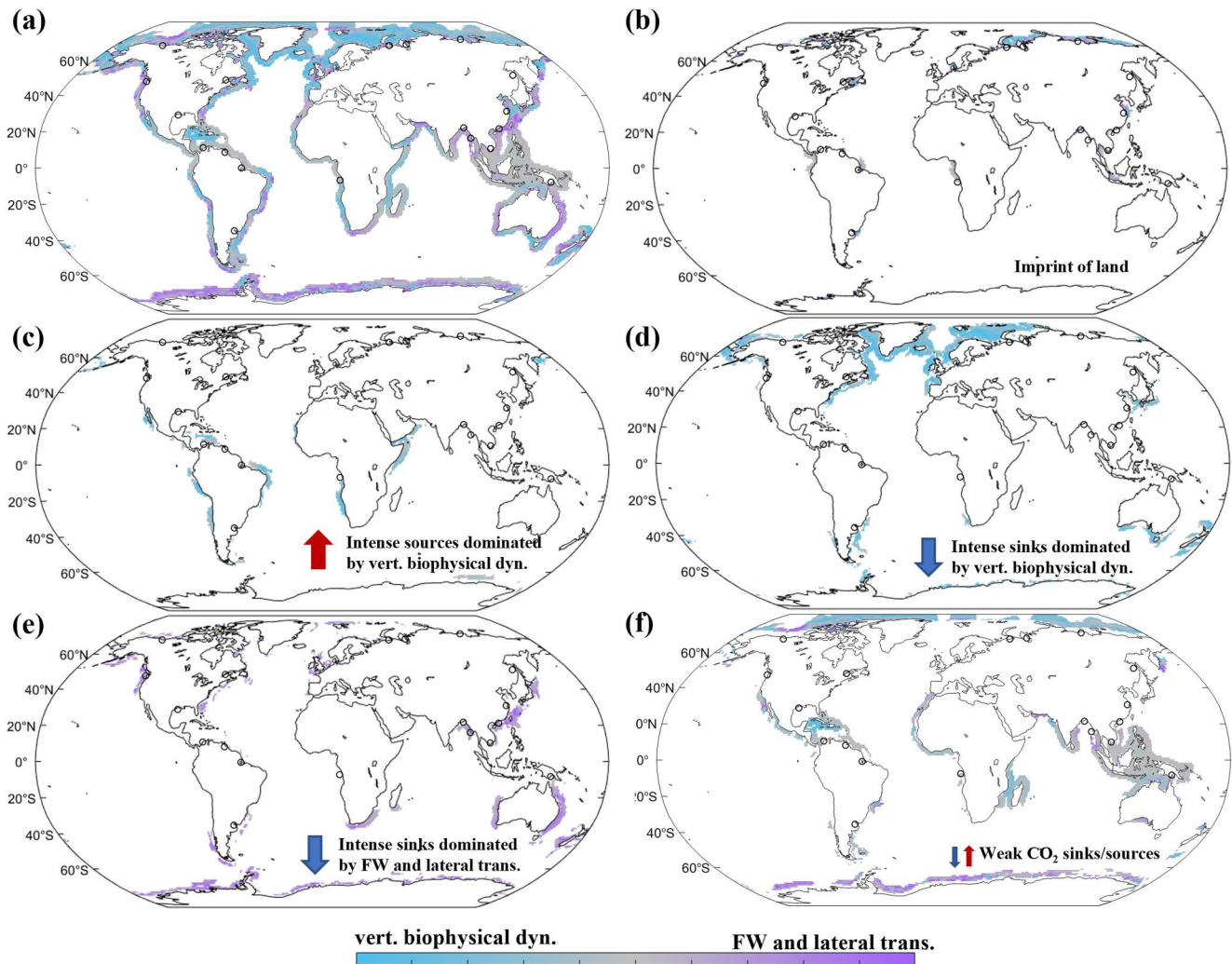
**Figure 4.** Processes controlling the annual average coastal ocean $CO_2$ response in the mixed layer depth (*CResponse*, which includes all $pCO_2$ changes whether they are equilibrated by the air-sea $CO_2$ flux or not, see Equation 2) in (a) the global coastal ocean and (b–f) in the five coastal systems identified in this study. Specifically, in (b) regions under imprint of land, (c) strong $CO_2$ sources dominated by the *vertical biophysical dynamics*, (d) strong $CO_2$ sinks dominated by the *vertical biophysical dynamics*, (e) strong $CO_2$ sinks dominated by the *freshwater and lateral transport* and (f) weak coastal $CO_2$ sources and sinks. Colors indicate the relative contributions from *vertical biophysical dynamics* (vert. biophysical dyn., in blue, balance between biological activity and vertical transport of chemical species), and the *freshwater and lateral transport* (FW and lateral trans., in purple, sum of dilution/concentration effects and lateral transport of chemical species). The *thermal effect* is not represented since its contribution to the annual average is near-zero (see Section 3.2 and Figure 2b). Results on all panels are averaged at 1° spatial resolutions for visibility. Black circles show the 20 largest annual average river runoffs.

*dynamics* (gray colors in Figure 5b). For instance, in the Amazon plume, $pCO_2$ and consequently the *CResponse* decreases from January to May ($\Delta CResponse = -54$ µatm, Figure 6b) due to the increase in river discharge, which peaks in May-June (Figure S13b in Supporting Information S1 and e.g., Liang et al., 2020) and leads to a dilution effect. This local $pCO_2$ anomaly tied to runoff is then horizontally transported offshore extending over the plume region (Figure 6d). Note that an important seasonal change in biological activity is also observed locally in the plume (Figure 3e) in response to seasonal changes in nutrient delivery.

### 3.2.2. Intense Coastal Sources Dominated by Vertical Biophysical Dynamics—Upwelling Systems

We then isolate regions that are strong $CO_2$ sources ($FCO_2 > 0.5$ mol C m$^{-2}$ yr$^{-1}$, Figure 1a) where *vertical biophysical dynamics* is the main controlling term of the annual average $CO_2$ response, with contributions that exceed the *freshwater and lateral transport* by about 70% (blue colors, Figure 4c). In these strong $CO_2$ sources, mainly located in tropical coastal regions, vertical dynamics exceed the biological drawdown (*vert. biophysical*
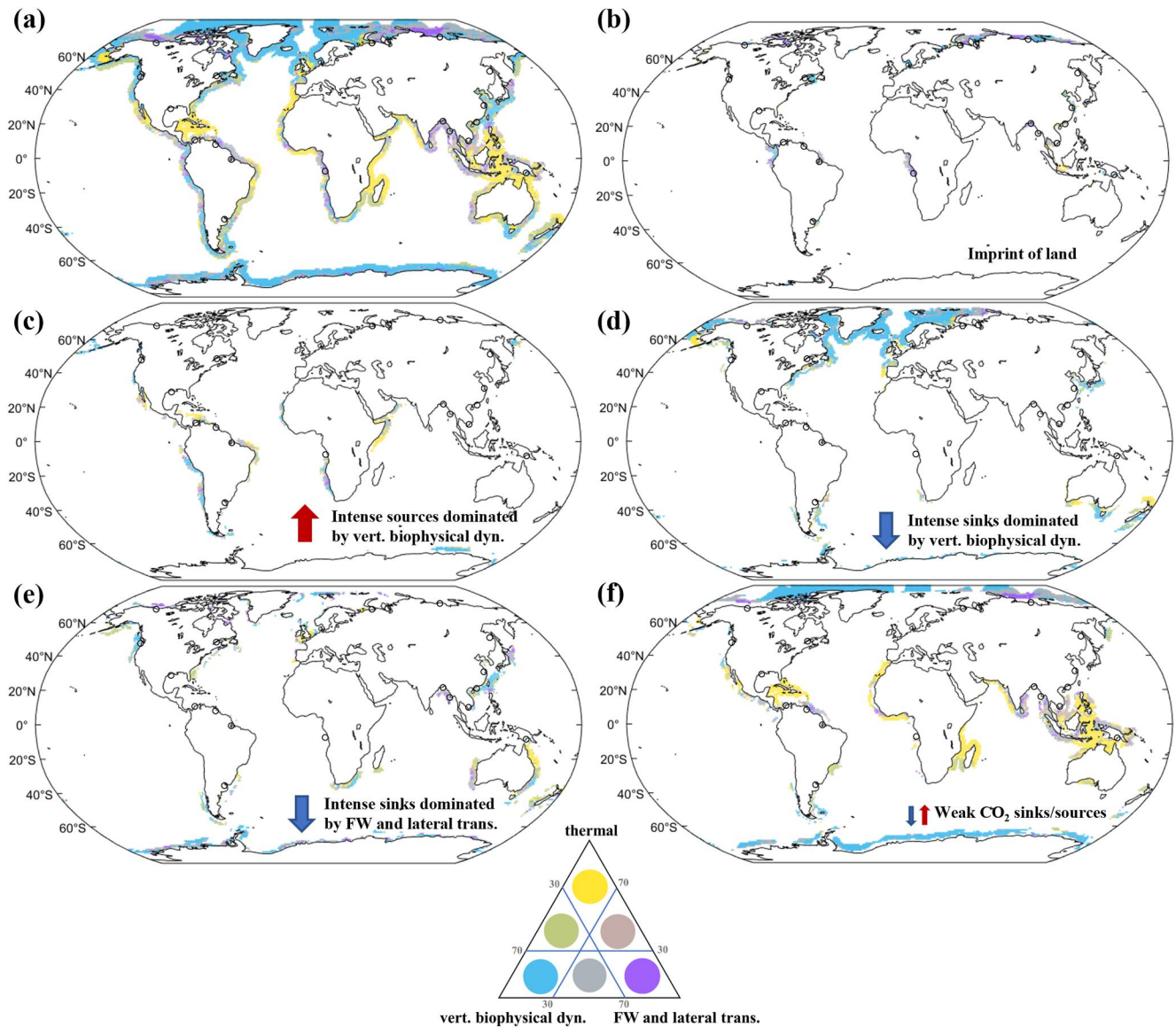
**Figure 5.** Processes controlling the seasonal cycle of the coastal ocean $CO_2$ response in the mixed layer depth (*CResponse*) in (a) the global coastal ocean and (b–f) in the five coastal systems identified in this study. Specifically, in (b) regions under imprint of land, (c) strong $CO_2$ sources dominated by the *vertical biophysical dynamics*, (d) strong $CO_2$ sinks dominated by the *vertical biophysical dynamics*, (e) strong $CO_2$ sinks dominated by the *freshwater and lateral transport* and (f) weak coastal $CO_2$ sources and sinks. Colors indicate the relative contributions from *vertical biophysical dynamics* (vert. biophysical dyn., in blue, balance between biological activity and vertical transport of chemical species), *freshwater and lateral transport* (FW and lateral trans., in purple, sum of dilution/concentration effects and lateral transport of chemical species) and *thermal changes* (thermal, in yellow). Results on all panels are averaged at 1° spatial resolutions for visibility. Black circles show the 20 largest annual mean river runoffs.

*dyn.* >0, Figures 2c, 2e, and 2g). Most of these tropical source regions correspond to upwelling systems, including the Californian, Peruvian, Moroccan, and South West Africa eastern upwelling Currents as well as the monsoon-driven upwelling system in the western Arabian sea (Figure 4c). In the Californian upwelling, for instance, the intense supply of deep carbon-enriched waters by vertical circulation yields an annual average increase in the $CO_2$ response of +347 µatm yr$^{-1}$ (spatially averaged median value of the *vert. biophysical dyn.* in Figure 2c). In this case, the upwelling-driven increase in $pCO_2$ (+956 µatm yr$^{-1}$ for *Vcirc*, Figure 2g) is partly compensated by the photosynthetic activity enabled by the upwelling of nutrient-rich waters, which decreases the $CO_2$ response by −609 µatm yr$^{-1}$ (*bio* in Figure 2e), and by the effect of *freshwater and lateral transport*, which further decreases $pCO_2$ by −103 µatm yr$^{-1}$ (+46 and −149 µatm yr$^{-1}$ for *FW* and *Hcirc*, respectively) (Figures 2f and 2h). As a
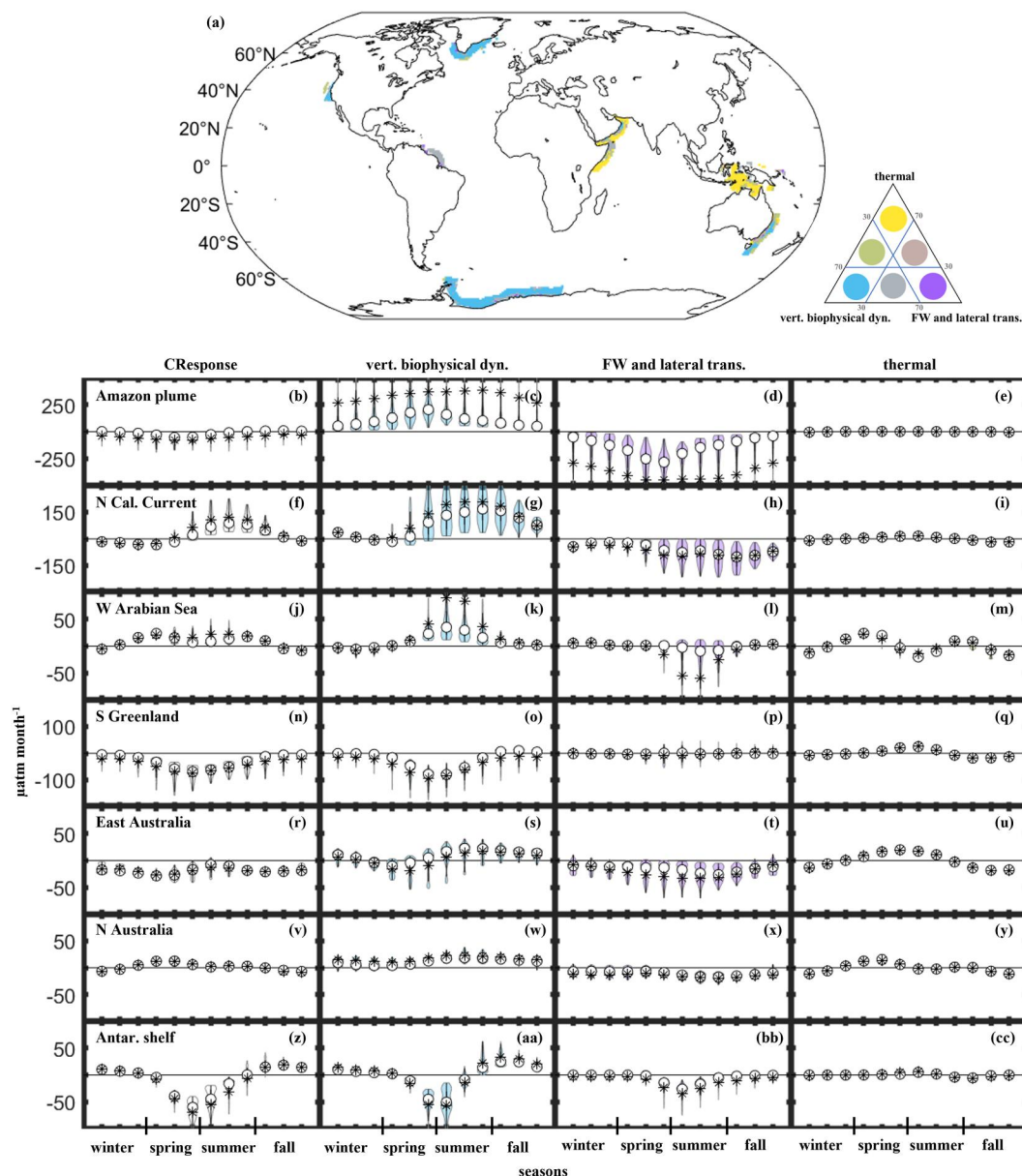
**Figure 6.** (a) Location of the different regions where we examine the seasonal cycle of the coastal ocean $CO_2$ response in the mixed layer depth. (b–cc) Seasonal cycle of *CResponse* and processes for seven coastal regions. The violins (10–90th percentile) represent the intra-spatial variability of each process within the region for each month. The medians and means are represented by circles and stars, respectively. A positive value corresponds to an increase in the *CResponse*. Winter corresponds to January (July), February (August), and March (September) in the Northern (Southern) hemisphere.

result of these physical and biological processes, the $pCO_2$ increases by +126 µatm $yr^{-1}$ over the course of the entire year, sustaining the intense outgassing of $CO_2$ in this region (Figures 1a and 4c).

The seasonality in upwelling systems can be controlled by either of the three processes (*thermal*, *vert. biophysical dyn.*, *FW and lateral trans.*) and the balance between them can be spatially heterogeneous (Figure 5c). In several upwelling systems, the *vertical biophysical dynamics* control the seasonality (e.g., in the northern of the California Current or in the Peruvian upwelling Current, blue colors in Figure 5c). For instance, in the northern Californian Current, the winter-to-summer increase in $pCO_2$ between January and July (Δ*CResponse* = +85 µatm, Figure 6f) follows the *vertical biophysical dynamics* (Figure 6g and blue colors in Figure 5c) in agreement with past studies (e.g., Brady et al., 2019; Turi et al., 2014). In this region, the *vertical biophysical*

*dynamics* shows a winter-to-summer increase in $pCO_2$, indicating that the vertical supply of carbon dominates over the biological drawdown associated with the upwelling event. In other upwelling regions or when the seasonal amplitude is low in upwelling systems, the $pCO_2$ seasonal change associated with the *vertical biophysical dynamics* can be compensated by the seasonal change in $pCO_2$ associated with other processes such as the seasonal change in *freshwater and lateral transport* inducing a dominance of the *thermal effect*. For instance, in the Western Arabian Sea, the summer Southwest monsoon upwelling increases $pCO_2$ (*vert. biophysical dyn.*, Figure 6k) but is largely offset by the reduction in $pCO_2$ tied to the alongshore transport of low $pCO_2$ waters (reduction in *FW and lateral trans.* term, Figure 6l). Because of this near complete compensation, the seasonality of the carbon response in this region largely follows the biannual SST peaks taking place in the spring and fall inter-monsoons (April and October, Figure 6m). In particular, $pCO_2$ decreases in summer due to the strong summertime upwelling of cold waters in the Western Arabian Sea (Schott & McCreary, 2001).

### 3.2.3. Intense Coastal Sinks Dominated by Vertical Biophysical Dynamics—Subpolar and Polar Systems

We then isolate coastal regions that are annual strong sinks ($FCO_2 < -0.5$ mol C m$^{-2}$ yr$^{-1}$, Figure 1a) where *vertical biophysical dynamics* is the main controlling term of the annual mean $CO_2$ response. These systems mainly regroup coastal regions located at subpolar and polar latitudes in the Northern Hemisphere. The behavior of the shelves surrounding Antarctica departs from the one described for northern polar systems. Indeed, this region falls into the category of weak $CO_2$ sources and sinks in this study and is thus discussed in Section 3.2.5. In polar and subpolar latitudes of the Northern Hemisphere, the biological drawdown exceeds the supply of $CO_2$ by vertical dynamics (*vert. biophysical dyn.* $<0$, Figure 2c, and blue color in Figure 4d). In South Greenland, for instance, biological activity yields a $pCO_2$ drawdown of $-571$ µatm yr$^{-1}$ (Figure 2e), which is only partly offset by the $+275$ µatm yr$^{-1}$ increase tied to the supply of carbon-rich water during winter mixing (Figure 2g). In this case, the *freshwater and lateral transport* play a minor role ($-11$ and $+6$ µatm yr$^{-1}$ for *FW* and *Hcirc*, respectively).

These polar and subpolar sink regions of the Northern Hemisphere are generally characterized by large seasonal flux amplitudes (root mean square, RMS, $FCO_2$ value $>0.8$ mol C m$^{-2}$ yr$^{-1}$) except at locations under sea-ice coverage (Figure 1c). The seasonality evolves from being purely controlled by *vertical biophysical dynamics* in polar systems (blue colors in Figure 5d) to being controlled by a combination of *vertical biophysical dynamics* and *thermal changes* in subpolar systems (blue and yellow colors in Figure 5d). For instance, in the polar South Greenland, which is a $CO_2$ sink throughout the year (spatially average $FCO_2$ value of $-4$ mol C m$^{-2}$ yr$^{-1}$), the winter-to-summer decline in $pCO_2$ ($\Delta CResponse = -64$ µatm from January to June, Figure 6n) is entirely explained by the *vertical biophysical dynamics* drawdown associated with the phytoplankton bloom in spring/early summer ($\Delta vert.\ biophysical\ dyn. = -78$ µatm month$^{-1}$ between January and June, Figure 6o), and later compensated by an increase associated with vertical mixing and a reduction in photosynthesis in fall/early winter ($\Delta CResponse = +74$ µatm from July to December, see e.g., Mann & Lazier, 2013; Sarmiento & Gruber, 2006; Sigman & Hain, 2012). The larger importance of *thermal changes* in subpolar regions, particularly in the Northern Hemisphere (RMS values of the *thermal effect* generally $>20$ µatm month$^{-1}$, Figure 3b and Text S5 in Supporting Information S1), is consistent with the larger SST variations at these latitudes, up to 20°C between winter and summer, compared to low and high latitudes regions (median RMS of generally $<15$ µatm month$^{-1}$) where seasonal SST variations can be as little as ~5°C at the equator.

### 3.2.4. Intense Coastal Sinks Dominated by Lateral Transport—Intracoastal Currents

We then isolate coastal regions that are characterized by annual average strong sinks ($FCO_2 < -0.5$ mol C m$^{-2}$ yr$^{-1}$, Figure 1a) primarily controlled by the *fresh water and lateral transport* term on annual average (purple color, Figure 4e). These features are mainly found in coastal regions with strong intracoastal currents, such as along the East and West coast of Australia, the East coast of the U.S., the coast of South East Africa as well as the East coast of China. These regions are characterized by intense intracoastal alongshore currents (Gulf stream, East Australian, Kuroshio, Leeuwin, and Agulhas Currents) that transport waters with a deficit in surface $pCO_2$ compared to local conditions. The intracoastal transport of water masses explains the atmospheric $CO_2$ uptake in these regions, for instance, when water that cooled traveling poleward did not have enough time to equilibrate with the atmosphere and therefore presented a $pCO_2$ deficit.

These regions show strong seasonal variability (RMS $>0.8$ mol C m$^{-2}$ yr$^{-1}$) but the processes controlling this seasonality vary across regions (Figure 5e). For instance, along the East coast of China, the *vertical biophysical*

*dynamics* tend to dominate the seasonal variability (blue colors, Figure 5e), while along the East and West coast of Australia as well as along the coast of South East Africa, the seasonal variability of the *CResponse* is driven by a mix between *thermal change* influence, change in horizontal circulation and the spring biological uptake, as exemplified along the East Australian Current (Figures 6r–6u).

### 3.2.5. Weak Coastal $CO_2$ Sources and Sinks

Finally, the fifth region type includes coastal regions with weak annual average fluxes (either sources or sink, absolute value $FCO_2 < 0.5$ mol C m$^{-2}$ yr$^{-1}$) and low seasonal amplitudes (RMS <0.8 mol C m$^{-2}$ yr$^{-1}$) that are generally found at tropical latitudes (Figures 1a and 1c). In these weak annual flux tropical regions, *freshwater and lateral transport* are either the main driver (purple color in Figure 4f) or are contributing equally with *vertical biophysical dynamics* to the annual average $CO_2$ response (gray colors in Figure 4f), while the weak seasonality is primarily controlled by *thermal changes* (yellow colors in Figure 5f). For instance, in the North of Australia, the low seasonal variability of the *freshwater and lateral transport* (possibly controlled by seasonal rainfall events) is compensated by the effect of *vertical biophysical dynamics*, and the low seasonal amplitude of the $FCO_2$ cycle ($\Delta CResponse = 18$ µatm from July to October, Figure 6v) therefore mimics that of the *thermal changes* both in timing and amplitude (Figure 6y). The thermal effect results from a typical seasonal SST rise throughout spring and summer, which decreases the $CO_2$ solubility and increases the surface water $pCO_2$, while the decrease in SST in autumn and winter leads to a $CO_2$ solubility increase and a decrease in surface water $pCO_2$ (e.g., Takahashi et al., 2009). Notable exceptions of coastal regions that are weak sources/sinks but exhibit different controls are the low $CO_2$ flux regions along the Antarctic shelf and at high latitudes of the Northern Hemisphere. The high latitude regions of the Northern Hemisphere, typically under sea-ice coverage all year round, tend to have the same behavior as intense polar coastal sink regions, a dominance of the biological uptake on both the annual average and seasonal $FCO_2$ variability (blue colors in Figures 4f and 5f). In contrast, the annual average $CO_2$ dynamics along the Antarctic shelf are controlled by the *freshwater and lateral transport* (purple color in Figures 4e and 4f). Here, the *vertical biophysical dynamics* term is very small (spatially averaged *vert. biophysical dyn.* = +48 µatm yr$^{-1}$, Figure 2c) because of the quasi compensation between the biological drawdown of $pCO_2$ (*bio* = −628 µatm yr$^{-1}$) and the contribution of vertical transport (*Vcirc* = +677 µatm yr$^{-1}$) associated with winter mixing and summer upwelling events in the Weddell, Ross and Kerguelen Plateau gyres (see e.g., Vernet et al., 2019). As a result of this weak effect of the *vertical biophysical dynamics*, the *freshwater and lateral transport* dominate the annual mean $CO_2$ flux in the shelves surrounding Antarctica, in response to the sea-ice dynamics (formation, transport and melting) and runoff effects (ice-shelf and iceberg melt, Figure S11b in Supporting Information S1). The seasonality of the Antarctic shelves is largely controlled by *vertical biophysical dynamics*, similar to the northern polar shelves (blue color in Figures 5e and 5f). Specifically, the seasonality in the Weddell gyre follows an intense and short-lived decline in $pCO_2$ in early summer due to the phytoplankton spring bloom (−45 µatm month$^{-1}$ in December, Figures 6z–6aa). In contrast to for instance the South Greenland case, however, $pCO_2$ in the Weddell gyre increases in summer/fall in response to *vertical biophysical dynamics* (+25 µatm month$^{-1}$ in April, Figure 6aa), likely due to the deepening of the mixed layer and local upwelling events that bring deep carbon rich water to the upper layer (e.g., Vernet et al., 2019) but only have a small influence of biological drawdown due to the light and iron limitation of phytoplanktonic growth (e.g., Martin et al., 1990).

## 4. Discussion

This study shows that the spatial distribution of coastal $CO_2$ sources and sinks, their intensities, and variability on a seasonal timescale result from the complex interplay between biological activity, oceanic circulation, thermal change, and freshwater influences (e.g., compensation between processes, indirect influence of one process on another, "memory" effects induced by lateral transport) in line with previous studies (e.g., Borges, 2005; Borges et al., 2005; Cai, 2011; Cai et al., 2006). We also show that the processes controlling the coastal surface ocean $pCO_2$ and air-sea $CO_2$ flux depend on the time scale (annual average vs. seasonal) and/or the region studied. However, we find patterns in the behavior of coastal systems that emerge from this complexity and can be used to identify distinct coastal regimes using a consistent quantitative approach across the global coastal ocean.

The model results echo with the concept of Cao et al. (2020) and Dai et al. (2022) in which the world's coastal ocean $CO_2$ flux dynamics can be organized into river-dominated ocean margins where the carbon fluxes are primarily controlled by terrestrial loads ("RiOMar's," McKee et al., 2004; Rabouille et al., 2001) and ocean-dominated margins where the carbon fluxes are primarily controlled by exchanges with the surrounding open
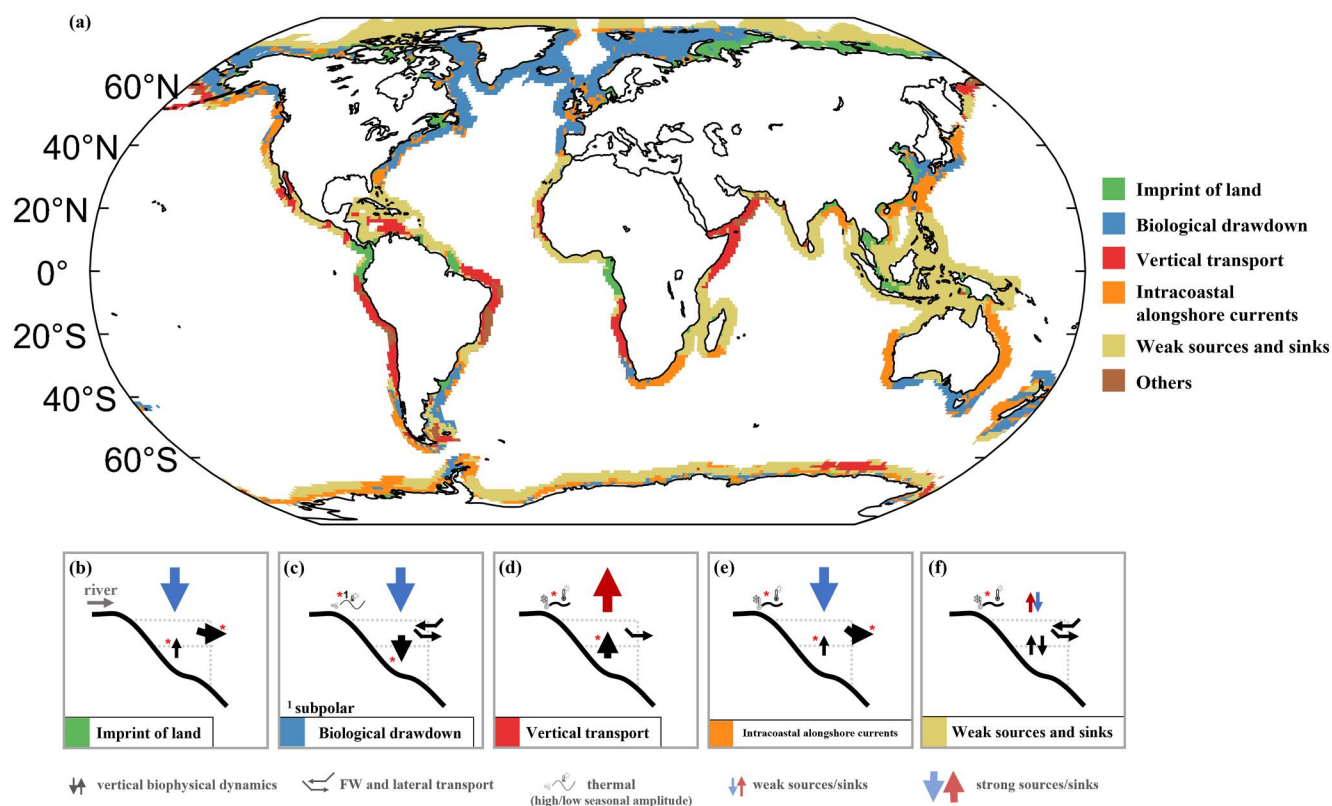
**Figure 7.** (a) Division of the coastal ocean into five coastal systems that present different key controls on the coastal $CO_2$ dynamics in the mixed layer depth (MLD). For each of these five categories is associated a sketch (b–f) that presents the main control on the annual average $CO_2$ sources/sinks and the variability on the seasonal timescale (red stars) in the MLD. Flux into the MLD increases *CResponse*.

ocean ("OceMar's," Dai et al., 2013, 2022). Coastal regions where the biogeochemical dynamics result from intense interactions with the adjacent open ocean have already been identified in the past and include the U.S East coast (e.g., Fennel & Wilkin, 2009; Laruelle et al., 2015) or the California Current (e.g., Frischknecht et al., 2018). The same is true for coastal regions influenced by the imprint of riverine plumes (e.g., the Amazon plume; Louchard et al., 2021). However, we find that the $CO_2$ dynamics is only clearly impacted by riverine inputs in a tiny portion of the global coastal area (<10%), which can consistently be mapped across the global ocean. As a result, and even if some of the regions act locally as very strong sinks (e.g., the mouth of the Amazon River), the overall global scale coastal $CO_2$ dynamics is not driven by these river-dominated ocean margins, which is in line with previous studies (e.g., Cai et al., 2006; Cotrim da Cunha et al., 2007; Wollast, 1998). In contrast, our results reinforce the conceptual view of the coastal $CO_2$ dynamics vastly dominated by strong exchanges with the open ocean or by the carbon dynamics within the coastal region itself. Based on a quantitative approach of the internal processes driving the $FCO_2$ dynamics, we thus divide the global coastal ocean into five types of coastal systems that, we believe, are more relevant in the light of the key external (both from the land and open ocean) and internal controls of the coastal $CO_2$ dynamics identified in this study. Indeed, in spite of their merits, the classification of K. Liu et al. (2010) for instance only defined generic types of climatology based coastal settings and the units of the MARCATS segmentation were delineated using first order physical and geomorphological static boundaries, both of which were static and not constrained by the spatiotemporal distribution of the physical and biogeochemical processes controlling the $CO_2$ dynamics in the global coastal ocean.

Our first category includes river plumes under land influence (using a SSS criteria), while the four other coastal types are defined based on the signs of their $CO_2$ flux (sources/sinks), their intensities (weak vs. strong sources/sinks) and the dominance of the *vertical biophysical dynamics* or the *freshwater and lateral transport* on annual average (Figure 7). Based on these criteria, the $CO_2$ dynamics in the coastal ocean is dominated by the imprint of land (coastal regions with important SSS anomalies compared with the adjacent open ocean, in green in Figure 7a), the biological drawdown (intense $CO_2$ sinks dominated by *vertical biophysical dynamics*, in blue), the

vertical transport (intense $CO_2$ sources dominated by *vertical biophysical dynamics*, in red), and intracoastal alongshore surface currents (intense $CO_2$ sinks dominated by *freshwater and lateral transport*, in orange). The last category groups weak $CO_2$ sources and sinks coastal regions dominated by *freshwater and lateral transport* and/or the *vertical biophysical dynamics* (in yellow). We also assign a class for coastal regions that do not fit into any of these categories (in brown, 2% total coastal surface). It should be noted that the classes described below cover the entirety of the global coastal ocean (excluding marginal seas) regardless of the performance of the model. As a consequence, regions where a significant mismatch exists between the $FCO_2$ simulated by the model and that calculated using the data product should be considered with caution. For instance, such regions include several temperate and sub-polar shelves located in the Northern Hemisphere (Figure 1), many of which are intense $CO_2$ sinks dominated by *vertical biophysical dynamics* as well as the Peruvian upwelling current, the West Arabian Sea, the Bay of Bengal, the Sea of Labrador, the coasts of New Zealand, Tropical East Pacific shelves and South East Asia, which had already been identified in Roobaert et al. (2022). Future model improvements may reveal even more complex dynamics in these areas and lead to an update of our classification.

*Coastal regions under the imprint of land* represent <10% of the coastal ocean and correspond to coastal regions under the strong influence of the land-derived inputs via river discharges such as the Amazon Plume, the Mackenzie River, or the Siberian coastal regions (green colors in Figure 7a). For most of these regions, the model simulates intense $CO_2$ sinks on their annual mean and their $CO_2$ response (annual average and seasonal variability, Figure 7b) resulting from the combined effects of (a) freshwater via dilution and the transport of these anomalies by horizontal circulation, and (b) biological uptake (e.g., at the mouth of the Amazon Plume) due to riverine nutrient inputs. Note that the use of SSS alone to determine the spatial extent of the influence of riverine inputs on the coastal ocean implies that this delineation is mostly determined by physics rather than the combined effect of physics and biogeochemistry, as is the case for the other classes. This approach may underestimate the full extent of the true influence of terrestrial inputs in some regions by ignoring the potential long-range transport and recycling of terrestrial nutrients and organic matter. A better constraint on these processes would require model sensitivity experiments without terrestrial influences.

*Coastal sinks dominated by the biological drawdown* correspond to intense $CO_2$ sinks ($FCO_2$ <−0.5 mol C m$^{-2}$ yr$^{-1}$) in "polar" and "subpolar" (following K. Liu et al., 2010) coastal regions (20% of coastal surface area; Figures 7a and 7c). Their intense annual average sink is controlled by the *vertical biophysical dynamics,* that is, the imbalance between biological activity and vertical transport. In polar regions, there is a clear dominance of biologically induced $CO_2$ uptake versus vertical carbon supply, while in subpolar coastal regions, the behavior is more heterogeneous but biologically induced $CO_2$ uptake versus vertical carbon supply tends to also dominate, as in polar regions (Figures 7a and 7c). Their seasonal variability is controlled by *vertical biophysical dynamics* in polar coastal regions but by a combination of *vertical biophysical dynamics* and *thermal changes* in subpolar coastal regions. Note that coastal regions located at high latitudes in the Northern Hemisphere and around Antarctica, which are characterized by weak $CO_2$ flux intensity (due to the presence of sea-ice most of the year or to large compensation between processes), are not included in the polar and subpolar categories described here but in the weak sources and sinks category (see details below).

*Coastal sources dominated by the vertical transport* correspond to intense $CO_2$ sources in coastal upwelling systems (10% of coastal surface area; Figures 7a and 7d), specifically regions known as Eastern boundary currents ("EBCs") and the northwestern Indian Ocean Arabian Sea's dominated by intense coastal upwelling during the summer monsoon. Similar to polar and subpolar regions, their $CO_2$ response is controlled by the *vertical biophysical dynamics*, but in this case the vertical transport exceeds the biological drawdown (Figures 7a and 7d). On seasonal timescales, the *vertical biophysical dynamics* also dominates but with a significant contribution of *thermal changes* and to a lesser extent lateral transport, although in some cases *thermal changes* can have a stronger impact. For instance, for the low source and low seasonal variability of the upwelling of the Arabian Sea's, due to the compensating effects of vertical and lateral exchanges, their seasonal dynamics is small and regulated by the thermal component that follows the biannual monsoon on a seasonal time scale.

*Coastal regions dominated by intracoastal alongshore currents* (17% total coastal surface area) broadly correspond to the Western Boundary Currents systems ("WBC") and the Leeuwin Current. They all reveal a strong annual average sink (e.g., the Agulhas Current, the East Australian Current, the Kuroshio Current) driven mostly by alongshore lateral transport (Figures 7a and 7e) suggesting that the coastal $CO_2$ dynamics is significantly controlled by non-local processes occurring upstream. The seasonal dynamics is also dominated by lateral

transport although at these shorter timescales, the local contribution of biology and thermal effects have a larger share in explaining the $CO_2$ air-sea exchange.

*Weak $CO_2$ sources and sinks coastal regions* (43% of the coastal surface area) are those corresponding to the "tropical" category in the K. Liu et al. classification (32% of coastal surface area) and to high latitude regions with very low flux intensity due to sea-ice coverage or compensation between opposing processes (11% of the coastal surface area). These regions are characterized by different dynamics, but they are grouped together here because of their small impact on the annual and seasonal variations in the atmospheric $CO_2$ budget (weak sources/sinks with weak seasonality). Overall, we note that the tropical regions falling in this category have their annual average $CO_2$ dynamics nearly equally dominated by the *freshwater and lateral transport* and the *vertical biophysical dynamics*. At the seasonal scale, their effects on the air-sea $CO_2$ exchange mirror each other in such a way that the seasonality is dominated by *thermal changes* despite being much dampened in these low latitude regions. Note that although we report the dominance of a thermal signal in the tropical coastal $CO_2$ seasonality, it should be remembered that most of these regions are characterized by a very small seasonal amplitude in this $CO_2$ signal. This finding should therefore rather be interpreted as another evidence of the nearly balanced dynamics between the *vertical biophysical dynamics* and the *freshwater and lateral transport* exchanges of carbon in the model. This category also includes coastal regions located at high latitudes of the Northern Hemisphere and the Antarctic shelf due to their low $CO_2$ fluxes on an annual average. In the northern hemisphere regions, the $CO_2$ seasonal and annual mean dynamics follow the one of polar regions, that is, a dominance of biological drawdown while the Antarctic shelf is mostly controlled by internal processes along the Antarctic circumpolar current.

This analysis of the $CO_2$ dynamics sheds a new light on the global coastal carbon cycle. First, our results further strengthen the notion that the coastal $CO_2$ dynamics are strongly linked to that of the open ocean. We advocate for instance that the coastal $CO_2$ dynamics in many polar regions and EBCs merely reflect the general ocean circulation, which involves vast exchanges through the deep open ocean. Furthermore, the analysis of the seasonal dynamics reveals that excluding regions with very small seasonal amplitude in the $CO_2$ dynamics such as the tropics, thermal changes are only significant contributors in subpolar regions and, to a lesser extent, in EBCs in some specific case of strong compensation between the other terms (e.g., the Arabian Sea).

## 5. Conclusions

Using the global ocean biogeochemical model MOM6-COBALT and the Takahashi et al. (1993) decomposition refined by Roobaert et al. (2022) to more robustly capture the highly variable coastal $CO_2$ dynamics, this study provides a global quantitative analysis of the mechanisms governing the distribution of the sea surface $CO_2$ sources and sinks, their intensities and seasonal variability in coastal regions worldwide. While the spatial resolution of the model can still not capture all small-scale ocean circulation processes, its ability to properly reproduce the $CO_2$ dynamics in vast portions of the global coastal ocean is demonstrated through a comparison with fluxes calculated using a state-of-the-art $FCO_2$ data product (Laruelle et al., 2017; Roobaert et al., 2019). We then quantified the respective contributions of freshwater inputs, biological activity as well as vertical and horizontal ocean transport to elucidate the spatial variability of the annual average $CO_2$ source/sink nature of the global coastal ocean. Moreover, we quantified the respective contributions of these same processes along with thermal effects to explain the seasonal variability of the global coastal $CO_2$ exchange. This study shows that the coastal $CO_2$ dynamics is vastly dominated by strong exchanges with the open ocean or by the internal carbon dynamics within the coastal region itself, the regions under strong imprint from the land only contributing locally. Based on our quantitative approach, a new delineation of the global coastal ocean was proposed, where five broad categories were mapped using the identified control mechanisms of the annual mean and seasonal $CO_2$ dynamics. Note that this new delineation of the coastal ocean into five categories covers the entire coastal domain (except marginal seas which were not investigated in this study) although some spatiotemporal model-data discrepancies are observed on the $CO_2$ flux and $pCO_2$ (Roobaert et al., 2022). Additional data should be collected in the future in regions void of data (e.g., in Indian ocean margins, upwelling currents) or periods of the years that are not covered to be evaluated if the data-model mismatch results from a poor performance of the model or the observation-based $pCO_2$ product against which the model is evaluated.

Our results also help speculate on the extent to which the coastal $FCO_2$ might have been impacted by changing nutrient inputs from the land, the main driver of a stronger anthropogenic perturbation in the shallow portion of the ocean than in the open ocean in box-model studies (e.g., Mackenzie et al., 2002; Rabouille et al., 2001; Ver

et al., 1999). Consistent with previous observational work (e.g., Dai et al., 2022; Roobaert et al., 2019), the present-day global coastal $CO_2$ sink is strongly dominated by polar regions, and we suggest that these coastal sinks dominated by the biological drawdown have so far only marginally been perturbed by changing nutrient inputs from the land (Lacroix, Ilyina, Mathis, et al., 2021; Terhaar et al., 2019). In the tropics, except for highly localized regions under direct influence of land-derived nutrient inputs, the weak $CO_2$ sources appear mostly driven by exchanges with the open ocean through vertical and horizontal transport, suggesting that their long-term $CO_2$ dynamics could have only marginally been altered by a changing biology. WBCs are mostly located in temperate regions, the latitudinal band that has experienced the largest relative increase in land-derived nutrient inputs over the last century. In these systems, however, we speculate that the dominance of strong intracoastal alongshore currents could significantly decrease the efficiency by which the enhanced biological carbon fixation can be exported to the deep. Overall, these patterns collectively support the hypothesis of a weak response of the coastal $CO_2$ uptake to changing nutrient inputs at the global scale (Lacroix, Ilyina, Laruelle, & Regnier, 2021; Regnier et al., 2013, 2022). In the future, our model-based approach could provide further insights into the extent to which anthropogenic perturbations have impacted the air-sea $CO_2$ exchange of the global coastal ocean. This will require extending our analysis of the physical and biogeochemical drivers of the coastal air-sea $CO_2$ exchange over longer timescales, from inter-annual variability to trends over the entire historical period (1850–present).

## Conflict of Interest

The authors declare no conflicts of interest relevant to this study.

## Data Availability Statement

The $FCO_2$ simulated by the MOM6-COBALT model use $\Delta pCO_2$ from the difference between the surface ocean $pCO_2$ simulated by MOM6-COBALT and the latitude-temporal varied $pCO_{2,air}$ dataset from the ESRL (Joos & Spahni, 2008). The observation-based $FCO_2$ is calculated using $\Delta pCO_2$ from the difference between the continuous monthly $pCO_2$ coastal-product of Laruelle et al. (2017) generated by a two-step artificial neural network interpolation technique (the Self Organizing map and Feed Forward Neural networks method) and observations extracted from the Surface Ocean $CO_2$ Atlas database version 4 (SOCATv4, Bakker et al., 2016). The $pCO_{2,air}$ derived from the SeaFlux product (Fay et al., 2021). For both products, $FCO_2$ is calculated using the k-relationship calculated in the model based on the quadratic parametrization of Wanninkhof (1992) and wind speeds from JRA55-do v1.3 (Tsujino et al., 2018). The sea-ice cover is from the monthly mean of the daily 0.25° dataset of Cavalieri et al. (1996) for the observation-based $FCO_2$, while it is modeled by the sea-ice model SIS2 in MOM6-COBALT (Adcroft et al., 2019).

## References

Abril, G., Libardoni, B. G., Brandini, N., Cotovicz, L. C., Medeiros, P. R. P., Cavalcante, G. H., & Knoppers, B. A. (2021). Thermodynamic uptake of atmospheric $CO_2$ in the oligotrophic and semiarid São Francisco estuary (NE Brazil). *Marine Chemistry*, *233*, 103983. https://doi.org/10.1016/j.marchem.2021.103983

Adcroft, A., Anderson, W., Balaji, V., Blanton, C., Bushuk, M., Dufour, C. O., et al. (2019). The GFDL global ocean and sea ice model OM4.0: Model description and simulation features. *Journal of Advances in Modeling Earth Systems*, *11*(10), 3167–3211. https://doi.org/10.1029/2019MS001726

Araujo, M., Noriega, C., Hounsou-gbo, G. A., Veleda, D., Araujo, J., Bruto, L., et al. (2017). A synoptic assessment of the Amazon river-ocean continuum during boreal autumn: From physics to plankton communities and carbon flux. *Frontiers in Microbiology*, *8*, 257293. https://doi.org/10.3389/fmicb.2017.01358

Arruda, R., Calil, P. H. R., Bianchi, A. A., Doney, S. C., Gruber, N., Lima, I., & Turi, G. (2015). Air-sea $CO_2$ fluxes and the controls on ocean surface $pCO_2$ seasonal variability in the coastal and open-ocean southwestern Atlantic Ocean: A modeling study. *Biogeosciences*, *12*(19), 5793–5809. https://doi.org/10.5194/bg-12-5793-2015

Bakker, D. C. E., Alin, S. R., Becker, M., Bittig, H. C., Castaño-Primo, R., Feely, R. A., et al. (2022). Surface Ocean $CO_2$ Atlas Database Version 2022 (SOCATv2022) (NCEI Accession 0253659) [Dataset]. *NOAA National Centers for Environmental Information*. https://doi.org/10.25921/1h9f-nb73

Bakker, D. C. E., Pfeil, B., Landa, C. S., Metzl, N., O'Brien, K. M., Olsen, A., et al. (2016). A multi-decade record of high-quality fCO2 data in version 3 of the Surface Ocean $CO_2$ Atlas (SOCAT) [Dataset]. *Earth System Science Data*, *8*(2), 383–413. https://doi.org/10.5194/essd-8-383-2016

Borges, A. V. (2005). Do we have enough pieces of the jigsaw to integrate $CO_2$ fluxes in the coastal ocean? *Estuaries*, *28*(1), 3–27. https://doi.org/10.1007/BF02732750

Borges, A. V., Delille, B., & Frankignoulle, M. (2005). Budgeting sinks and sources of $CO_2$ in the coastal ocean: Diversity of ecosystem counts. *Geophysical Research Letters*, *32*(14), L14601. https://doi.org/10.1029/2005GL023053

Bourgeois, T., Orr, J. C., Resplandy, L., Terhaar, J., Ethé, C., Gehlen, M., & Bopp, L. (2016). Coastal-ocean uptake of anthropogenic carbon. *Biogeosciences*, *13*(14), 4167–4185. https://doi.org/10.5194/bg-13-4167-2016

Brady, R. X., Lovenduski, N. S., Alexander, M. A., Jacox, M., & Gruber, N. (2019). On the role of climate modes in modulating the air-sea $CO_2$ fluxes in eastern boundary upwelling systems. *Biogeosciences*, *16*(2), 329–346. https://doi.org/10.5194/bg-16-329-2019

Cai, W.-J, Dai, M., & Wang, Y. (2006). Air-sea exchange of carbon dioxide in ocean margins: A province-based synthesis. *Geophysical Research Letters*, *33*(12), 2–5. https://doi.org/10.1029/2006GL026219

Cai, W.-J. (2011). Estuarine and coastal ocean carbon paradox: $CO_2$ sinks or sites of terrestrial carbon incineration? *Annual Review of Marine Science*, *3*(1), 123–145. https://doi.org/10.1146/annurev-marine-120709-142723

Cao, Z., Yang, W., Zhao, Y., Guo, X., Yin, Z., Du, C., et al. (2020). Diagnosis of $CO_2$ dynamics and fluxes in global coastal oceans. *National Science Review*, *7*(4), 786–797. https://doi.org/10.1093/nsr/nwz105

Cavalieri, D., Parkinson, C., Gloersen, P., & Zwally, H. J. (1996). Sea ice concentrations from Nimbus-7 SMMR and DMSP SSM/I passive microwave data [Dataset]. *National Snow and Ice Data Center, Digital media*. https://nsidc.org/data/nsidc-0051/versions/1

Chau, T. T. T., Gehlen, M., & Chevallier, F. (2022). A seamless ensemble-based reconstruction of surface ocean p$CO_2$ and air-sea $CO_2$ fluxes over the global coastal and open oceans. *Biogeosciences*, *19*(4), 1087–1109. https://doi.org/10.5194/bg-19-1087-2022

Chen, C. T. A., & Borges, A. V. (2009). Reconciling opposing views on carbon cycling in the coastal ocean: Continental shelves as sinks and near-shore ecosystems as sources of atmospheric $CO_2$. *Deep Sea Research Part II: Topical Studies in Oceanography*, *56*(8–10), 578–590. https://doi.org/10.1016/j.dsr2.2009.01.001

Chen, C. T. A., Huang, T. H., Chen, Y. C., Bai, Y., He, X., & Kang, Y. (2013). Air-sea exchanges of $CO_2$ in the world's coastal seas. *Biogeosciences*, *10*(10), 6509–6544. https://doi.org/10.5194/bg-10-6509-2013

Chen, S., & Hu, C. (2019). Environmental controls of surface water p$CO_2$ in different coastal environments: Observations from marine buoys. *Continental Shelf Research*, *183*, 73–86. https://doi.org/10.1016/j.csr.2019.06.007

Cotrim da Cunha, L., Buitenhuis, E. T., Le Quéré, C., Giraud, X., & Ludwig, W. (2007). Potential impact of changes in river nutrient supply on global ocean biogeochemistry. *Global Biogeochemical Cycles*, *21*(4), GB4007. https://doi.org/10.1029/2006GB002718

Dai, M., Cao, Z., Guo, X., Zhai, W., Liu, Z., Yin, Z., et al. (2013). Why are some marginal seas sources of atmospheric $CO_2$? *Geophysical Research Letters*, *40*(10), 2154–2158. https://doi.org/10.1002/grl.50390

Dai, M., Su, J., Zhao, Y., Hofmann, E. E., Cao, Z., Cai, W.-J., et al. (2022). Carbon fluxes in the coastal ocean: Synthesis, boundary processes and future trends. *Annual Review of Earth and Planetary Sciences*, *50*(1), 593–626. https://doi.org/10.1146/annurev-earth-032320-090746

Ducklow, H., & McCallister, S. (2004). The biogeochemistry of carbon dioxide in the coastal oceans. In *The sea* (Vol. 13).

Fay, A. R., Gregor, L., Landschützer, P., McKinley, G. A., Gruber, N., Gehlen, M., et al. (2021). SeaFlux: Harmonization of air-sea $CO_2$ fluxes from surface p$CO_2$ data products using a standardized approach [Dataset]. *Earth System Science Data*, *13*(10), 4693–4710. https://doi.org/10.5194/essd-13-4693-2021

Fennel, K., & Wilkin, J. (2009). Quantifying biological carbon export for the northwest North Atlantic continental shelves. *Geophysical Research Letters*, *36*(18), L18605. https://doi.org/10.1029/2009GL039818

Frankignoulle, M., & Borges, A. V. (2001). European continental shelf as a significant sink for atmospheric carbon dioxide. *Global Biogeochemical Cycles*, *15*(3), 569–576. https://doi.org/10.1029/2000GB001307

Frischknecht, M., Münnich, M., & Gruber, N. (2018). Origin, transformation, and fate: The three-dimensional biological pump in the California Current System. *Journal of Geophysical Research: Oceans*, *123*(11), 7939–7962. https://doi.org/10.1029/2018JC013934

Joos, F., & Spahni, R. (2008). Rates of change in natural and anthropogenic radiative forcing over the past 20,000 years [Dataset]. *Proceedings of the National Academy of Sciences of the United States of America*, *105*(5), 1425–1430. https://doi.org/10.1073/pnas.0707386105

Kang, Y., Pan, D., Bai, Y., He, X., Chen, X., Chen, C. T. A., & Wang, D. (2013). Areas of the global major river plumes. *Acta Oceanologica Sinica*, *32*(1), 79–88. https://doi.org/10.1007/s13131-013-0269-5

Lacroix, F., Ilyina, T., & Hartmann, J. (2020). Oceanic $CO_2$ outgassing and biological production hotspots induced by pre-industrial river loads of nutrients and carbon in a global modeling approach. *Biogeosciences*, *17*(1), 55–88. https://doi.org/10.5194/bg-17-55-2020

Lacroix, F., Ilyina, T., Laruelle, G. G., & Regnier, P. (2021). Reconstructing the preindustrial coastal carbon cycle through a global ocean circulation model: Was the global continental shelf already both autotrophic and a $CO_2$ sink? *Global Biogeochemical Cycles*, *35*(2), e2020GB006603. https://doi.org/10.1029/2020GB006603

Lacroix, F., Ilyina, T., Mathis, M., Laruelle, G. G., & Regnier, P. (2021). Historical increases in land-derived nutrient inputs may alleviate effects of a changing physical climate on the oceanic carbon cycle. *Global Change Biology*, *27*(21), 5491–5513. https://doi.org/10.1111/gcb.15822

Landschützer, P., Laruelle, G. G., Roobaert, A., & Regnier, P. (2020). A uniform p$CO_2$ climatology combining open and coastal oceans. *Earth System Science Data*, *12*(4), 2537–2553. https://doi.org/10.5194/essd-12-2537-2020

Laruelle, G. G., Dürr, H. H., Lauerwald, R., Hartmann, J., Slomp, C. P., Goossens, N., & Regnier, P. (2013). Global multi-scale segmentation of continental and coastal waters from the watersheds to the continental margins. *Hydrology and Earth System Sciences*, *17*(5), 2029–2051. https://doi.org/10.5194/hess-17-2029-2013

Laruelle, G. G., Dürr, H. H., Slomp, C. P., & Borges, A. V. (2010). Evaluation of sinks and sources of $CO_2$ in the global coastal ocean using a spatially-explicit typology of estuaries and continental shelves. *Geophysical Research Letters*, *37*(15), L15607. https://doi.org/10.1029/2010GL043691

Laruelle, G. G., Landschützer, P., Gruber, N., Tison, J. L., Delille, B., & Regnier, P. (2017). Global high-resolution monthly p$CO_2$ climatology for the coastal ocean derived from neural network interpolation [Dataset]. *Biogeosciences*, *14*(19), 4545–4561. https://doi.org/10.5194/bg-14-4545-2017

Laruelle, G. G., Lauerwald, R., Pfeil, B., & Regnier, P. (2014). Regionalized global budget of the $CO_2$ exchange at the air-water interface in continental shelf seas. *Global Biogeochemical Cycles*, *28*(11), 1199–1214. https://doi.org/10.1002/2014GB004832

Laruelle, G. G., Lauerwald, R., Rotschi, J., Raymond, P. A., Hartmann, J., & Regnier, P. (2015). Seasonal response of air-water $CO_2$ exchange along the land-ocean aquatic continuum of the northeast North American coast. *Biogeosciences*, *12*(5), 1447–1458. https://doi.org/10.5194/bg-12-1447-2015

Lauderdale, J. M., Dutkiewicz, S., Williams, R. G., & Follows, M. J. (2016). Quantifying the drivers of ocean-atmosphere $CO_2$ fluxes. *Global Biogeochemical Cycles*, *30*(7), 983–999. https://doi.org/10.1002/2016GB005400

Lefèvre, N., Diverrès, D., & Gallois, F. (2010). Origin of $CO_2$ undersaturation in the western tropical Atlantic. *Tellus Series B Chemical and Physical Meteorology*, *62*(5), 595. https://doi.org/10.1111/j.1600-0889.2010.00475.x

Liang, Y. C., Lo, M. H., Lan, C. W., Seo, H., Ummenhofer, C. C., Yeager, S., et al. (2020). Amplified seasonal cycle in hydroclimate over the Amazon river basin and its plume region. *Nature Communications*, *11*(1), 4390. https://doi.org/10.1038/s41467-020-18187-0

Liao, E., Resplandy, L., Liu, J., & Bowman, K. W. (2020). Amplification of the ocean carbon sink during El Niños: Role of poleward Ekman transport and influence on atmospheric $CO_2$. *Global Biogeochemical Cycles*, *34*(9), e2020GB006574. https://doi.org/10.1029/2020GB006574

Liu, K., Atkinson, L., Quiñones, R., & Talaue-McManus, L. (2010). *Carbon and nutrient fluxes in continental margins*. Springer Science & Business Media. https://doi.org/10.1007/978-3-540-92735-8

Liu, X., Dunne, J. P., Stock, C. A., Harrison, M. J., Adcroft, A., & Resplandy, L. (2019). Simulating water residence time in the coastal ocean: A global perspective. *Geophysical Research Letters*, *46*(23), 13910–13919. https://doi.org/10.1029/2019GL085097

Louchard, D., Gruber, N., & Münnich, M. (2021). The impact of the Amazon on the biological pump and the air-sea $CO_2$ balance of the western tropical Atlantic. *Global Biogeochemical Cycles*, *35*(6), e2020GB006818. https://doi.org/10.1029/2020GB006818

Mackenzie, F. T., De Carlo, E. H., & Lerman, A. (2012). Coupled C, N, P, and O biogeochemical cycling at the land-ocean interface. In *Treatise on estuarine and coastal science* (Vol. 5). https://doi.org/10.1016/B978-0-12-374711-2.00512-X

Mackenzie, F. T., Ver, L. M., & Lerman, A. (2002). Century-scale nitrogen and phosphorus controls of the carbon cycle. *Chemical Geology*, *190*(1–4), 13–32. https://doi.org/10.1016/S0009-2541(02)00108-0

Mann, K. H., & Lazier, J. R. N. (2013). Dynamics of marine ecosystems: Biological-physical interactions in the oceans. In *Dynamics of marine ecosystems: Biological-physical interactions in the oceans* (3rd ed.). https://doi.org/10.1002/9781118687901

Martin, J. H., Fitzwater, S. E., & Gordon, R. M. (1990). Iron deficiency limits phytoplankton growth in Antarctic waters. *Global Biogeochemical Cycles*, *4*(1), 5–12. https://doi.org/10.1029/GB004I001P00005

Mathis, M., Logemann, K., Maerz, J., Lacroix, F., Hagemann, S., Chegini, F., et al. (2022). Seamless integration of the coastal ocean in global marine carbon cycle modeling. *Journal of Advances in Modeling Earth Systems*, *14*(8), e2021MS002789. https://doi.org/10.1029/2021MS002789

McKee, B. A., Aller, R. C., Allison, M. A., Bianchi, T. S., & Kineke, G. C. (2004). Transport and transformation of dissolved and particulate materials on continental margins influenced by major rivers: Benthic boundary layer and seabed processes. *Continental Shelf Research*, *24*(7–8), 899–926. https://doi.org/10.1016/j.csr.2004.02.009

Nakaoka, S. I., Aoki, S., Nakazawa, T., Hashida, G., Morimoto, S., Yamanouchi, T., & Yoshikawa-Inoue, H. (2006). Temporal and spatial variations of oceanic $pCO_2$ and air-sea $CO_2$ flux in the Greenland Sea and the Barents Sea. *Tellus Series B Chemical and Physical Meteorology*, *58*(2), 148–161. https://doi.org/10.1111/j.1600-0889.2006.00178.x

Orr, J. C., & Epitalon, J. M. (2015). Improved routines to model the ocean carbonate system: Mocsy 2.0. *Geoscientific Model Development*, *8*(3), 485–499. https://doi.org/10.5194/gmd-8-485-2015

Rabouille, C., Mackenzie, F. T., & Ver, L. M. (2001). Influence of the human perturbation on carbon, nitrogen, and oxygen biogeochemical cycles in the global coastal ocean. *Geochimica et Cosmochimica Acta*, *65*(21), 3615–3641. https://doi.org/10.1016/S0016-7037(01)00760-8

Regnier, P., Friedlingstein, P., Ciais, P., Mackenzie, F. T., Gruber, N., Janssens, I. A., et al. (2013). Anthropogenic perturbation of the carbon fluxes from land to ocean. *Nature Geoscience*, *6*(8), 597–607. https://doi.org/10.1038/ngeo1830

Regnier, P., Resplandy, L., Najjar, R. G., & Ciais, P. (2022). The land-to-ocean loops of the global carbon cycle. *Nature*, *603*(7901), 401–410. https://doi.org/10.1038/s41586-021-04339-9

Resplandy, L., Hogikyan, A., Müller, J. D., Najjar, R. G., Bange, H. W., Bianchi, D., et al. (2024). A synthesis of global coastal ocean greenhouse gas fluxes. *Global Biogeochemical Cycles*, *38*(1), e2023GB007803. https://doi.org/10.1029/2023GB007803

Roobaert, A., Laruelle, G. G., Landschützer, P., Gruber, N., Chou, L., & Regnier, P. (2019). The spatiotemporal dynamics of the sources and sinks of $CO_2$ in the global coastal ocean. *Global Biogeochemical Cycles*, *33*(12), 1693–1714. https://doi.org/10.1029/2019GB006239

Roobaert, A., Laruelle, G. G., Landschützer, P., & Regnier, P. (2018). Uncertainty in the global oceanic $CO_2$ uptake induced by wind forcing: Quantification and spatial analysis. *Biogeosciences*, *15*(6), 1701–1720. https://doi.org/10.5194/bg-15-1701-2018

Roobaert, A., Regnier, P., Landschützer, P., & Laruelle, G. G. (2024). A novel sea surface $pCO_2$-product for the global coastal ocean resolving trends over 1982–2020. *Earth System Science Data*, *16*(1), 421–441. https://doi.org/10.5194/essd-16-421-2024

Roobaert, A., Resplandy, L., Laruelle, G. G., Liao, E., & Regnier, P. (2022). A framework to evaluate and elucidate the driving mechanisms of coastal sea surface $pCO_2$ seasonality using an ocean general circulation model (MOM6-COBALT). *Ocean Science*, *18*(1), 1–34. https://doi.org/10.5194/os-2021-70

Sarmiento, J. L., & Gruber, N. (2006). Ocean biogeochemical dynamics. In *Carbon*. Princeton University Press. https://doi.org/10.1063/1.2754608

Schott, F. A., & McCreary, J. P. (2001). The monsoon circulation of the Indian Ocean. *Progress in Oceanography*, *51*(1), 1–123. https://doi.org/10.1016/S0079-6611(01)00083-0

Shadwick, E. H., Thomas, H., Azetsu-Scott, K., Greenan, B. J. W., Head, E., & Horne, E. (2011). Seasonal variability of dissolved inorganic carbon and surface water $pCO_2$ in the Scotian Shelf region of the Northwestern Atlantic. *Marine Chemistry*, *124*(1–4), 23–37. https://doi.org/10.1016/j.marchem.2010.11.004

Shadwick, E. H., Thomas, H., Comeau, A., Craig, S. E., Hunt, C. W., & Salisbury, J. E. (2010). Air-sea $CO_2$ fluxes on the Scotian Shelf: Seasonal to multi-annual variability. *Biogeosciences*, *7*(11), 3851–3867. https://doi.org/10.5194/bg-7-3851-2010

Sigman, D. M., & Hain, M. P. (2012). The biological productivity of the ocean. *Nature Education Knowledge*, *3*(6), 1–16.

Stock, C. A., Dunne, J. P., Fan, S., Ginoux, P., John, J., Krasting, J. P., et al. (2020). Ocean biogeochemistry in GFDL's Earth System Model 4.1 and its response to increasing atmospheric $CO_2$. *Journal of Advances in Modeling Earth Systems*, *12*(10), e2019MS002043. https://doi.org/10.1029/2019MS002043

Stock, C. A., Dunne, J. P., & John, J. G. (2014). Global-scale carbon and energy flows through the marine planktonic food web: An analysis with a coupled physical-biological model. *Progress in Oceanography*, *120*, 1–28. https://doi.org/10.1016/j.pocean.2013.07.001

Takahashi, T., Olafsson, J., Goddard, J. G., Chipman, D. W., & Sutherland, S. C. (1993). Seasonal variation of $CO_2$ and nutrients in the high-latitude surface oceans: A comparative study. *Global Biogeochemical Cycles*, *7*(4), 843–878. https://doi.org/10.1029/93GB02263

Takahashi, T., Sutherland, S. C., Wanninkhof, R., Sweeney, C., Feely, R. A., Chipman, D. W., et al. (2009). Climatological mean and decadal change in surface ocean $pCO_2$, and net sea-air $CO_2$ flux over the global oceans. *Deep Sea Research Part II: Topical Studies in Oceanography*, *56*(8-10), 554–577. https://doi.org/10.1016/j.dsr2.2008.12.009

Terhaar, J., Orr, J. C., Ethé, C., Regnier, P., & Bopp, L. (2019). Simulated Arctic Ocean response to doubling of riverine carbon and nutrient delivery. *Global Biogeochemical Cycles*, *33*(8), 1048–1070. https://doi.org/10.1029/2019GB006200

Tsujino, H., Urakawa, S., Nakano, H., Small, R. J., Kim, W. M., Yeager, S. G., et al. (2018). JRA-55 based surface dataset for driving ocean–sea-ice models (JRA55-do) [Dataset]. *Ocean Modelling*, *130*, 79–139. https://doi.org/10.1016/j.ocemod.2018.07.002

Turi, G., Lachkar, Z., & Gruber, N. (2014). Spatiotemporal variability and drivers of $pCO_2$ and air-sea $CO_2$ fluxes in the California Current System: An eddy-resolving modeling study. *Biogeosciences*, *11*(3), 671–690. https://doi.org/10.5194/bg-11-671-2014

Valerio, A. M., Kampel, M., Ward, N. D., Sawakuchi, H. O., Cunha, A. C., & Richey, J. E. (2021). $CO_2$ partial pressure and fluxes in the Amazon River plume using in situ and remote sensing data. *Continental Shelf Research*, *215*, 104348. https://doi.org/10.1016/j.csr.2021.104348

Ver, L. M. B., Mackenzie, F. T., & Lerman, A. (1999). Carbon cycle in the coastal zone: Effects of global perturbations and change in the past three centuries. *Chemical Geology*, *159*(1–4), 283–304. https://doi.org/10.1016/S0009-2541(99)00042-X

Vernet, M., Geibert, W., Hoppema, M., Brown, P. J., Haas, C., Hellmer, H. H., et al. (2019). The Weddell Gyre, Southern Ocean: Present knowledge and future challenges. *Reviews of Geophysics*, *57*(3), 623–708. https://doi.org/10.1029/2018RG000604

Walsh, J. J. (1988). *On the nature of the continental shelves*. Academic Press. https://doi.org/10.1016/c2013-0-11665-0

Wanninkhof, R. (1992). Relationship between wind speed and gas exchange. *Journal of Geophysical Research*, *97*(92), 7373–7382. https://doi.org/10.1029/92JC00188

Wanninkhof, R. (2014). Relationship between wind speed and gas exchange over the ocean revisited. *Limnology and Oceanography: Methods*, *12*(C5), 351–362. https://doi.org/10.1029/92JC0018

Wolf-Gladrow, D. A., Zeebe, R. E., Klaas, C., Körtzinger, A., & Dickson, A. G. (2007). Total alkalinity: The explicit conservative expression and its application to biogeochemical processes. *Marine Chemistry*, *106*(1–2), 287–300. https://doi.org/10.1016/j.marchem.2007.01.006

Wollast, R. (1998). Evaluation and comparison of the global carbon cycle in the coastal zone and in the open ocean. In *The sea* (pp. 213–252).

Yasunaka, S., Murata, A., Watanabe, E., Chierici, M., Fransson, A., van Heuven, S., et al. (2016). Mapping of the air-sea $CO_2$ flux in the Arctic Ocean and its adjacent seas: Basin-wide distribution and seasonal to interannual variability. *Polar Science*, *10*(3), 323–334. https://doi.org/10.1016/j.polar.2016.03.006

## References From the Supporting Information

Conway, T. J., Tans, P. P., Waterman, L. S., Thoning, K. W., Kitzis, D. R., Masarie, K. A., & Zhang, N. (1994). Evidence for interannual variability of the carbon cycle from the National Oceanic and Atmospheric Administration/Climate Monitoring and Diagnostics Laboratory Global Air Sampling Network. *Journal of Geophysical Research*, *99*(D11), 22831–22855. https://doi.org/10.1029/94jd01951

Dee, D. P., Uppala, S. M., Simmons, A. J., Berrisford, P., Poli, P., Kobayashi, S., et al. (2011). The ERA-Interim reanalysis: Configuration and performance of the data assimilation system. *Quarterly Journal of the Royal Meteorological Society*, *137*(656), 553–597. https://doi.org/10.1002/qj.828

Garcia, H. E., Locarnini, R. A., Boyer, T. P., Antonov, J. I., Baranova, O. K., Zweng, M. M., et al. (2013a). *World Ocean Atlas 2013. Volume 3, Dissolved oxygen, apparent oxygen utilization, and oxygen saturation*. NOAA Atlas NESDIS (Vol. 75, p. 27). Ocean Climate Laboratory, National Oceanographic Data Center. https://doi.org/10.7289/V5XG9P2W

Garcia, H. E., Locarnini, R. A., Boyer, T. P., Antonov, J. I., Baranova, O. K., Zweng, M. M., et al. (2013b). *World Ocean atlas 2013, Volume 4, Dissolved inorganic nutrients (phosphate, nitrate, silicate)*. NOAA Atlas NESDIS (Vol. 76, p. 25). Ocean Climate Laboratory, National Oceanographic Data Center. https://doi.org/10.7289/V5J67DWD

Gregor, L., & Gruber, N. (2021). OceanSODA-ETHZ: A global gridded data set of the surface ocean carbonate system for seasonal to decadal studies of ocean acidification. *Earth System Science Data*, *13*(2), 777–808. https://doi.org/10.5194/essd-13-777-2021

Ho, D. T., Wanninkhof, R., Schlosser, P., Ullman, D. S., Hebert, D., & Sullivan, K. F. (2011). Toward a universal relationship between wind speed and gas exchange: Gas transfer velocities measured with $^3He/SF_6$ during the Southern Ocean Gas Exchange Experiment. *Journal of Geophysical Research*, *116*(7), C00F04. https://doi.org/10.1029/2010JC006854

Khatiwala, S., Tanhua, T., Mikaloff Fletcher, S., Gerber, M., Doney, S. C., Graven, H. D., et al. (2013). Global ocean storage of anthropogenic carbon. *Biogeosciences*, *10*(4), 2169–2191. https://doi.org/10.5194/bg-10-2169-2013

Lauvset, S. K., Key, R. M., Olsen, A., Van Heuven, S., Velo, A., Lin, X., et al. (2016). A new global interior ocean mapped climatology: The 1° × 1° GLODAP version 2. *Earth System Science Data*, *8*(2), 325–340. https://doi.org/10.5194/essd-8-325-2016

Locarnini, R. A., Mishonov, A. V., Antonov, J. I., Boyer, T. P., Garcia, H. E., Baranova, O. K., et al. (2013). *World ocean atlas 2013. Volume 1, Temperature*, NOAA Atlas NESDIS (Vol. 73, p. 40). Ocean Climate Laboratory, National Oceanographic Data Center. https://doi.org/10.7289/V55X26VD

Masarie, K. A., Hall, F. G., Collatz, G. J., Meeson, B. W., Los, S. O., Brown De Colstoun, E., & Landis, D. R. (2012). ISLSCP II Globalview: Atmospheric $CO_2$ concentrations [Dataset]. *ORNL DAAC*. https://doi.org/10.3334/ORNLDAAC/1111

Mayorga, E., Seitzinger, S. P., Harrison, J. A., Dumont, E., Beusen, A. H., Bouwman, A. F., et al. (2010). Global nutrient export from WaterSheds 2 (NEWS 2): Model development and implementation. *Environmental Modelling & Software*, *25*(7), 837–853. https://doi.org/10.1016/j.envsoft.2010.01.007

Olsen, A., Key, R. M., van Heuven, S., Lauvset, S. K., Velo, A., Lin, X., et al. (2016). The Global Ocean Data Analysis Project version 2 (GLODAPv2) – An internally consistent data product for the world ocean. *Earth System Science Data*, *8*, 297–323. https://doi.org/10.5194/essd-8-297-2016

Weiss, R. F. (1974). Carbon dioxide in water and seawater: The solubility of a non-ideal gas. *Marine Chemistry*, *2*(3), 203–215. https://doi.org/10.1017/CBO9781107415324.004

Zweng, M. M., Reagan, J. R., Antonov, J. I., Locarnini, R. A., Mishonov, A. V., Boyer, T. P., et al. (2013). World ocean atlas 2013. Volume 2: Salinity. In S. Levitus & A. Mishonov (Eds.), *NOAA Atlas NESDIS* (Vol. 74, p. 39). Ocean Climate Laboratory, National Oceanographic Data Center. https://doi.org/10.7289/V5251G4D